

Geochemistry, Geophysics, Geosystems®





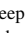



RESEARCH ARTICLE

10.1029/2022GC010791

Diverse Origins of Gases From Mud Volcanoes and Seeps in Tectonically Fragmented Terrane

Key Points:

- Mud volcanoes and gas seeps provide rapid access to probing subsurface fluid characteristics in tectonically active regions
- Thermogenic methane constitutes a major component of hydrocarbons and forms at temperatures of 99°–260°C
- A wide spectrum of geochemical characteristics indicates diverse formation mechanisms and conditions that constrain gas and water origins

Yueh-Ting Lin¹, Douglas Rumble², Edward D. Young³, Jabrane Labidi^{3,4} , Tzu-Hsuan Tu^{1,5} , Jhen-Nien Chen¹ , Thomas Pape⁶ , Gerhard Bohrmann⁶ , Saulwood Lin⁷, Li-Hung Lin^{1,8} , and Pei-Ling Wang^{7,8}

¹Department of Geosciences, National Taiwan University, New Taipei, Taiwan, ²Geophysical Laboratory, Carnegie Institution for Science, Washington, DC, USA, ³Department of Earth, Planetary and Space Sciences, University of California, Los Angeles, Los Angeles, CA, USA, ⁴Université de Paris Cité, Institut de Physique du Globe de Paris, CNRS, Paris, France, ⁵Department of Oceanography, National Sun Yat-Sen University, Kaohsiung City, Taiwan, ⁶MARUM – Center for Marine Environmental Sciences and Faculty of Geosciences, University of Bremen, Bremen, Germany, ⁷Institute of Oceanography, National Taiwan University, New Taipei, Taiwan, ⁸Research Center for Future Earth, National Taiwan University, New Taipei, Taiwan

Supporting Information:

Supporting Information may be found in the online version of this article.

Correspondence to:

L.-H. Lin and P.-L. Wang,
lhlin@ntu.edu.tw;
plwang@ntu.edu.tw

Citation:

Lin, Y.-T., Rumble, D., Young, E. D., Labidi, J., Tu, T.-H., Chen, J.-N., et al. (2023). Diverse origins of gases from mud volcanoes and seeps in tectonically fragmented terrane. *Geochemistry, Geophysics, Geosystems*, 24, e2022GC010791. <https://doi.org/10.1029/2022GC010791>

Received 15 NOV 2022

Accepted 17 AUG 2023

Author Contributions:

Conceptualization: Yueh-Ting Lin, Douglas Rumble, Li-Hung Lin, Pei-Ling Wang

Data curation: Yueh-Ting Lin, Douglas Rumble, Edward D. Young, Jabrane Labidi, Thomas Pape, Gerhard Bohrmann, Pei-Ling Wang

© 2023 The Authors. *Geochemistry, Geophysics, Geosystems* published by Wiley Periodicals LLC on behalf of American Geophysical Union. This is an open access article under the terms of the [Creative Commons Attribution-NonCommercial-NoDerivs License](https://creativecommons.org/licenses/by-nc-nd/4.0/), which permits use and distribution in any medium, provided the original work is properly cited, the use is non-commercial and no modifications or adaptations are made.

Abstract Identification of methane origins remains a challenging work as current diagnostic signals are often not sufficient to resolve individual formation and post-formation processes. To address such a knowledge gap in a tectonically active and fragmented terrain, samples from mud volcanoes, gas seeps, and springs distributed along structural features onshore and offshore of Taiwan were analyzed for their isotopic compositions of methane, nitrogen, helium, dissolved inorganic carbon, CO₂, and water. Our analyses yielded $\Delta^{13}\text{CH}_3\text{D}$ and $\Delta^{12}\text{CH}_2\text{D}_2$ values ranging between +1.9‰ and +7.8‰ and between +3.0‰ and +19.9‰, respectively. A portion of the samples were characterized by values that represent the thermodynamic equilibrium at temperatures of 99°–260°C. These temperature estimates, together with the bulk isotopic compositions and local geothermal gradients (25°–30°C/km), suggest that methane was formed by thermal maturation of organic matter at depths of 2–9 km below the land surface and channeled upward along faults. Other samples were found to deviate from equilibrium by varying degrees. Considering the geological background, helium isotopic ratios, and nitrogen isotopologue compositions, and methanogens detected at some sites, these gases are either abiotic in origin or a mixture of microbial and thermogenic sources. Regardless of whether the equilibrium of methane isotopologues was reached, few sites hosted by sedimentary formations were characterized by mantle-like helium signatures, indicating decoupled origins and potential degassing of helium from the relic igneous source. Overall, these results suggest the extraction of methane and other gases from multiple depths from strata fragmented by fault displacement in an active orogenic belt.

Plain Language Summary Mud volcanoes and gas seeps are distributed primarily in active tectonic regimes and represent the surface expression of subsurface fracture networks. They provide rapid access to probing subsurface characteristics for the generations of methane, other gases, and water. Identifying the exact mechanisms of methane formation remains a challenging work due to the lack of diagnostic signals with sufficient resolving power. This study employed a wide range of isotopic tools to constrain the origins of gases and water from mud volcanoes and seeps in Taiwan, where dual subductions and associated arc-continent collision between the Philippine Sea and Eurasian plates have enabled the plumbing of gases and water in accordance with structure development and stratum deformation. Our results reveal a spectrum of geochemical characteristics that point to diverse formation mechanisms and conditions. In particular, deeply sourced thermogenic methane (from depths of 2–9 km) appears to constitute a major gas component at most sites, and is mixed by various degrees with abiotic methane pertinent to igneous bodies emplaced during subduction/collision, or microbial methane generated at shallow depths. Overall, the results address the temporal and spatial variations in gas origins prone to terrain fragmentation and dynamic structural control associated with mountain building.

1. Introduction

Methane is the main gas component associated with petroleum and coal systems (Lundegard et al., 2000). Three major mechanisms have been suggested for its formation, including biological production from CO₂ and methylated

Formal analysis: Yueh-Ting Lin, Douglas Rumble, Edward D. Young, Jabrane Labidi, Tzu-Hsuan Tu, Jhen-Nien Chen, Li-Hung Lin, Pei-Ling Wang
Funding acquisition: Saulwood Lin, Li-Hung Lin, Pei-Ling Wang
Investigation: Yueh-Ting Lin, Douglas Rumble, Jabrane Labidi, Tzu-Hsuan Tu, Jhen-Nien Chen, Thomas Pape, Gerhard Bohrmann, Saulwood Lin, Li-Hung Lin, Pei-Ling Wang
Methodology: Yueh-Ting Lin, Douglas Rumble, Edward D. Young, Jabrane Labidi, Li-Hung Lin, Pei-Ling Wang
Supervision: Li-Hung Lin, Pei-Ling Wang
Validation: Li-Hung Lin, Pei-Ling Wang
Writing – original draft: Yueh-Ting Lin, Douglas Rumble, Edward D. Young, Jabrane Labidi, Thomas Pape, Gerhard Bohrmann, Li-Hung Lin, Pei-Ling Wang
Writing – review & editing: Yueh-Ting Lin, Douglas Rumble, Edward D. Young, Jabrane Labidi, Tzu-Hsuan Tu, Jhen-Nien Chen, Thomas Pape, Gerhard Bohrmann, Saulwood Lin, Li-Hung Lin, Pei-Ling Wang

compounds, stepwise thermal degradation of complex organic matters, and to a lesser extent, the Fischer-Tropsch Type reaction catalyzed by metals or sulfide minerals (Kietäväinen & Purkamo, 2015; Schoell, 1988; Stolper et al., 2014). Identifying the exact mechanisms and quantifying their fluxes from individual sources would greatly enhance our understanding of carbon cycling between reservoirs and their impact on future climate.

Mud volcanoes and seeps represent the surface expression of subsurface fracture networks and are considered to be effective channels of methane emission (Etiope, 2009; Kopf, 2003). Gases (predominantly hydrocarbons), water, and unconsolidated sediments originating from deep environments migrate upward due to gravitational instability and overpressurization driven by rapid burial and fault displacement (Carson & Sreaton, 1998), facilitating the minimum alteration of gas during channel transport, and the direct methane emissions into the atmosphere or seawater. Therefore, the geochemical characteristics of methane (e.g., abundance and isotopic composition) could potentially serve as an indicator of methane formation conditions, and the connectivity and extent of fractures in the crustal plumbing system (Mazzini & Etiope, 2017; Milkov & Etiope, 2018).

Methane isotopic compositions ($^{13}\text{C}/^{12}\text{C}$ and $^2\text{H}/^1\text{H}$) and abundance ratios as compared to higher hydrocarbons (C_1/C_2^+) are conventionally used to characterize methane origins (e.g., Bernard et al., 1977; Whiticar, 1999). This principle stems from experimental and field observations that constrain various degrees of isotopic fractionations and abundance ratios for different methane-formation mechanisms (Milkov & Etiope, 2018). These fingerprints are not unequivocal, as they are subject to further alteration caused by secondary processes, such as mixing, migration, and microbial oxidation (e.g., Bernard et al., 1977; Whiticar, 1999). The advancement of mass spectrometric techniques has enabled the measurement of two doubly substituted isotopologues ($^{13}\text{CH}_3\text{D}$ and $^{12}\text{CH}_2\text{D}_2$) at high precision (Young et al., 2016). The isotopologue approach provides a direct means to assess whether the methane has reached isotopic equilibrium (with coherent temperature estimates from two thermometers), overcoming the potential bias derived from the abundance of single doubly substituted isotopologue quantified by either mass or optic spectroscopy (Douglas et al., 2017; Ono et al., 2014; Young et al., 2016). Furthermore, the approach adds two additional constraints to conventional mixing models based on mass conservation, thereby facilitating coherent reservoir or process mixing models among different isotopic signals and better identification of end components. Finally, the gas origins could better be resolved with additional isotopic fingerprints of the constituent gases. While helium isotope ratios are conventionally exploited to differentiate mantle from crust and atmospheric sources (Poreda & Craig, 1989), the abundances of rare nitrogen isotopologues emerge as a sensitive indicator to track the cycling of air-derived nitrogen that could be falsely identified as the mantle nitrogen using the bulk nitrogen isotopic compositions (Labidi & Young, 2022). The approaches arise from the observation that mantle-derived $^{15}\text{N}/^{14}\text{N}$ abundances (from mid-ocean ridges and plumes) are consistent with the stochastic distribution for the intramolecular equilibrium, and are greatly distinctive from atmospheric nitrogen (Labidi et al., 2020a). These results combined with bulk nitrogen isotopic compositions and noble gas ratios enable us to trace nitrogen cycling associated with subduction and hydrothermal circulation potentially impacted by air contamination, as well as the identification of the primordial mantle (Labidi & Young, 2022; Labidi et al., 2020a, 2021). As terranes associated with subduction systems are fragmented by faulting and magmatism, gases that originate from multiple sources likely have distinctive combined isotopic patterns. The integration of multiple isotopic fingerprints (bulk and isotopologue) for specific geological occurrences offers insights into the gas formation, mixing, and alteration that have rarely been explored.

This study aims to determine the origins of methane from mud volcanoes and seeps onshore and offshore Taiwan by combining the abundances of rare methane and nitrogen isotopologues, and bulk isotopic compositions of helium, methane, dissolved inorganic carbon (DIC), CO_2 , and water. The study materials were chosen to take advantage of Taiwan's unique tectonic setting, at the intersection of dual subduction systems between the Eurasian and Philippine Sea plates (Lallemand, 2016). Mud volcanoes/seeps are associated with different structural features in different geological units, providing ideal opportunities to probe gas reservoirs in fragmented subsurface environments. These isotopic results were integrated with geological characteristics to address the mechanisms and potential depths of methane formation, and post-formation mixing and alteration.

2. Site Background

Taiwan is located in an active tectonic setting, at the boundary between the Philippine Sea plate and the Eurasian plate (Suppe, 1984; Teng & Lin, 2004). Major structures are oriented roughly northeast-southwest as a result of compression driven by the convergence and collision between the Luzon arc and the Eurasian continent. Geological

units on land, from west to east, include the Coastal Plain, the Western Foothills, the Hsuehshan Range, the Central Range (Backbone Range), the Longitudinal Valley, and the Coastal Range (Teng & Lin, 2004). A developing accretionary wedge is located offshore of southwestern Taiwan and features ridges and pockmarks (bathymetric depressions often interpreted as the signature of seafloor fluid transport) that have been postulated to extend from corresponding structures on land (Figure S1 in Supporting Information S1, C. S. Liu et al., 1997). Seismic surveys across the transect between Taiwan and the Eurasian continent reveal two structural domains (active and passive continental margins) separated by a projected deformation front that represents the extension of the Manila Trench (A. T. Lin et al., 2008). The active margin is further composed of the Upper Slope unit to the east, where mud diapirs predominate, and the Lower Slope unit to the west, where anticlinal ridges have formed (S. C. Chen et al., 2014; Y. Wang et al., 2022). Numerous mud volcanoes and seeps are distributed along faults or near anticlinal axes in southwestern and eastern Taiwan, and offshore southwestern Taiwan (Chao et al., 2011; N. C. Chen et al., 2017; Sun et al., 2010). Field sites investigated here are distributed near, or along structures, including the Chukou fault, Chishan fault, Gutingeng anticline, blind structures in the Coastal Plain, Longitudinal Valley fault, volcanic complexes, and the Formosa and Four Way Closure ridges offshore southwestern Taiwan (Figure S1 and Table S1 in Supporting Information S1). A more detailed description of the site background is given in the Supporting Information S1.

3. Materials and Methods

3.1. Field Sampling and Sample Processing

A total of 31 gas and water samples were collected from 23 mud volcanoes, gas seeps, and boreholes (Table S1 in Supporting Information S1). For most samples, gases were collected directly from bubbling features with the most vigorous activity. Sites AT and YSES are boreholes connected with a gas-water separator. Site GI-03 was an artisan well with vigorous bubbling, whereas site GI-01 was a pond (episodically flooded with seawater) with several bubbling features. To perform sampling at most sites, gases were drained into 50 mL gas-tight, pre-evacuated glass bottles with two stopcocks connected to a funnel. The funnel was first placed above bubbling features and filled with water. Water in the funnel was replaced gradually with the exsolved gases. The gases were used to purge the connecting tubing five times, and drained into pre-evacuated glass bottles (Figure S2 in Supporting Information S1). Sampling procedures were adjusted for three sites (YSES, WD, and AT). For samples from sites YSES and AT, gases discharged from the gas-water separator were directly diverted into pre-evacuated glass bottles. For samples from site WD, high erupting activities and outflowing water temperatures (63°C) prohibited direct sampling access. Therefore, mud and water flowing to the rim of the affected area were drained into serum bottles without headspace and capped with blue butyl rubber stoppers. Gases were extracted by connecting the sample bottles with pre-evacuated glass bottles. A total of five replicate bottles were collected for multiple gas analyses.

Offshore gas samples were collected from sediment cores drilled into gas-hydrate bearing zones at Formosa Ridge (site FR) and Four Way Closure Ridge (site FWCR) with the seafloor drill rig MARUM-MeBo200 during cruise SO266 with *R/V SONNE* (Bohrmann et al., 2023). Sediment cores dedicated to gas sampling were collected with pressure core samplers (Pape et al., 2017) and kept under in situ pressure during core retrieval. During onboard gas sampling, the pressure core was first depressurized slowly while monitoring the gas pressure. Gases were collected into stainless steel cylinders when the incremental gas pressure increased abruptly (up to 725 psi), an indicator of hydrate dissociation.

For all sites, water temperatures were measured on-site. Water samples were collected in 50 mL tubes and centrifuged at a speed of 10,000 ×g for 20 min. The supernatant was filtered through 0.22 μm pore-sized cellulose membranes and stored with no headspace at room temperature.

3.2. Sample Analyses

CH₄, C₂H₆, C₃H₈, and CO₂ concentrations were analyzed using a gas chromatograph (GC; 6890N, Agilent Technologies) with a flame ionization detector, and a thermal conductivity detector in line with a Porapak Q column using helium as the carrier gas. DIC concentrations were analyzed on CO₂ gases exsolved from water acidified with phosphoric acid (5%) using a CO₂ analyzer (Aurora 1030, O.I. Analytical). The reported gas abundances were corrected for the air assuming that oxygen measured was derived from the air and the N₂/O₂ ratio is 3.7. Since all samples were collected in five replicates, the sample was discarded if the air constituted the main component of the gases.

Carbon isotopic compositions of CH₄, DIC, and CO₂ were measured with a MAT253 isotope ratio mass spectrometer equipped with a GC IsoLink (Thermo Fisher Scientific) hosted at the National Taiwan University. The isotopic compositions are expressed in δ notation using the following equation:

$$\delta^{13}\text{C} = (R_{\text{sample}} / R_{\text{standard}} - 1) \times 1000\text{‰} \quad (1)$$

where R is ¹³C/¹²C, and the standard is Vienna Pee Dee Belemnite (VPDB).

For noble gas analyses, gases were introduced into a preline system for purification and separation. Helium isotopic ratios (³He/⁴He) and neon concentrations were measured using a helium isotope mass spectrometer (Helix, Thermo Scientific) in line with a quadrupole mass spectrometer (QMS200, Pfeiffer Vacuum). Helium ratios were calibrated against the standard atmospheric helium (Mishima et al., 2018) and a standard with a ³He/⁴He ratio 20.4 times of the atmospheric ratio (R_a) provided by the University of Tokyo (Sano et al., 2008), whereas neon concentrations and He/Ne ratios were calibrated against the air. Helium isotope ratios are expressed relative to the air using the following equation:

$$R/R_a = (^3\text{He}/^4\text{He})_{\text{sample}} / (^3\text{He}/^4\text{He})_{\text{atmosphere}} \quad (2)$$

where R and R_a are the ³He/⁴He ratios of sample and atmospheric helium, respectively.

Hydrogen and oxygen isotope compositions of water were measured using an Off-Axis Integrated Cavity Output Spectrometer (Los Gatos Research). The isotopic compositions are expressed in δ notation (Equation 1) with reference to VSMOW (Vienna Standard Mean Ocean Water).

Typical analytical uncertainties were 5% for gas concentrations, 2% for DIC concentrations, 0.2‰ for δ¹³C values, 0.2‰ for δ¹⁸O_{H₂O} values, 1.0‰ for δ²H_{H₂O} values, and 2% for ³He/⁴He. The detection limits for gas abundances and DIC concentrations were 10 ppmv, and 0.05 mM, respectively.

For methane isotopologues, currents of ¹²CH₄⁺, ¹³CH₄⁺, ¹²CH₃D⁺, ¹³CH₃D⁺, and ¹²CH₂D₂⁺ were measured using the Panorama (Nu Instruments) at the University of California at Los Angeles following established protocols (Giunta et al., 2019; Young et al., 2016, 2017). The mass resolving power of the spectrometer was equal to, or greater than 40,000, allowing for the resolution of two mass-18 isotopologues, ¹³CH₃D and ¹²CH₂D₂. Methane was purified using a GC equipped with two packed columns filled with 5A molecular sieve and HayeSepD porous polymer using helium as the carrier gas. Purified methane was collected, transferred, and expanded into the sample bellows connected to the mass spectrometer. In general, ¹²CH₃D⁺/¹²CH₄⁺ and ¹²CH₂D₂⁺/¹²CH₄⁺ ratios, and ¹³CH₄⁺/¹²CH₄⁺ and ¹³CH₃D/¹²CH₄⁺ ratios were measured with more than 20 blocks of data acquisition. In each block, alternating measurements on 20 samples and 21 standards were cycled every 30 s. Data were further integrated over individual blocks. The bulk isotopic compositions are adopted from ¹³CH₄⁺/¹²CH₄⁺ and ¹²CH₃D⁺/¹²CH₄⁺, and expressed in δ notation (δ¹³C and δ²H referenced to VPDB and VSMOW, respectively; Equation 1), whereas the isotopologue abundances are shown as uppercase delta values, defined as

$$\Delta^{13}\text{CH}_3\text{D} = \left[(^{13}\text{CH}_3\text{D}/^{12}\text{CH}_4)_{\text{sample}} / (^{13}\text{CH}_3\text{D}/^{12}\text{CH}_4)_{\text{stochastic}} - 1 \right] \times 1000\text{‰} \quad (3)$$

$$\Delta^{12}\text{CH}_2\text{D}_2 = \left[(^{12}\text{CH}_2\text{D}_2/^{12}\text{CH}_4)_{\text{sample}} / (^{12}\text{CH}_2\text{D}_2/^{12}\text{CH}_4)_{\text{stochastic}} - 1 \right] \times 1000\text{‰} \quad (4)$$

where the ratio of the isotopologues under stochastic conditions was calculated using the bulk isotope composition. Typical internal uncertainties for Δ¹³CH₃D, and Δ¹²CH₂D₂ values were less than ±0.2‰ and ±0.6‰ 1σ, respectively (Young et al., 2016, 2017).

The equilibrium temperatures were calculated following the relationship described in Young et al. (2016, 2017):

$$\Delta^{13}\text{CH}_3\text{D} \approx 1000 \times \ln \left(1 + 0.0355502/T - 433.038/T^2 + 1270210.0/T^3 - 5.94804 \times 10^8/T^4 + 1.196630 \times 10^{11}/T^5 - 9.0723 \times 10^{12}/T^6 \right) \quad (5)$$

$$\Delta^{12}\text{CH}_2\text{D}_2 \approx 1000 \times \ln \left(1 + 0.183798/T - 785.483/T^2 + 1056280.0/T^3 + 9.37307 \times 10^7/T^4 - 8.919480 \times 10^{10}/T^5 + 9.901730 \times 10^{12}/T^6 \right) \quad (6)$$

where T is in Kelvin.

Nitrogen isotopologues for five samples (sites KTL-02, WSD-01, AT, GI-01, and GI-03) were also determined. In short, nitrogen was purified on the same preline system as methane (Young et al., 2016). The abundances of $^{14}\text{N}^{14}\text{N}^+$, $^{14}\text{N}^{15}\text{N}^+$, and $^{15}\text{N}^{15}\text{N}^+$ ions were measured at a mass resolving power of approximately 50,000 (Labidi & Young, 2022). Data are expressed as $\delta^{15}\text{N}$ (Equation 1; referenced to the air) and Δ_{30} (Yeung et al., 2017):

$$\Delta_{30} = \left(\frac{{}^{30}\text{R}}{({}^{15}\text{R})^2} - 1 \right) \times 1000\text{‰} \quad (7)$$

where ${}^{30}\text{R} = {}^{15}\text{N}^{15}\text{N}/{}^{14}\text{N}^{14}\text{N}$ and ${}^{15}\text{R} = {}^{15}\text{N}/{}^{14}\text{N}$.

4. Results

Gas compositions and isotopic compositions are shown in Figure 1 and Table S1 in Supporting Information S1. Gases in most samples were dominated by methane (>75%), with the exception of CO_2 -rich (>80%) gases from sites CLS and CLP (Table S1 in Supporting Information S1). Minor amounts of ethane (0.1%–1.7%) and propane (0%–0.4%) were observed in all samples. Bulk carbon and hydrogen isotopic compositions of methane spanned over a wide range ($\delta^{13}\text{C}_{\text{CH}_4}$ from -86.9‰ to -16.7‰ and $\delta^2\text{H}_{\text{CH}_4}$ from -206.4‰ to -78.4‰) with the majority of $\delta^{13}\text{C}_{\text{CH}_4}$ and $\delta^2\text{H}_{\text{CH}_4}$ values clustering between -39.3‰ and -30.7‰ and between -167.8‰ and -138.5‰ , respectively. While DIC $\delta^{13}\text{C}$ values were from -29.5‰ to $+30.6\text{‰}$, DIC concentrations varied considerably between 0.4 and 271.3 mM. For comparison, $\delta^{13}\text{C}_{\text{CO}_2}$ values ranged from -24.8‰ to $+20.5\text{‰}$.

The $\Delta^{13}\text{CH}_3\text{D}$ and $\Delta^{12}\text{CH}_2\text{D}_2$ values ranged between $+1.90\text{‰}$ and $+7.83\text{‰}$ and between $+2.97\text{‰}$ and $+19.85\text{‰}$, respectively (Figure 2; Table S2 in Supporting Information S1). Among all samples, eight (CLP, CLS, KTL, SYNH-02, WSD-01, WD, AT, and LS) had isotopologue abundances consistent with the thermodynamic equilibrium at temperatures ranging from 23°C to 260°C (Table S2 in Supporting Information S1). Other samples were characterized by values deviating from the equilibrium by varying degrees (Figure 2). The $\delta^{15}\text{N}$ and Δ_{30} values ranged between -2.1‰ and $+3.6\text{‰}$, and between 1.8 and 16.4‰ relative to the stochastic distribution of isotopologues, respectively (Figure S3 and Table S3 in Supporting Information S1).

Helium isotopic compositions spanned from 0.1 to 5.4 Ra. Eight samples possessed $^3\text{He}/^4\text{He}$ ratios of >1 Ra (Figure 3; Table S4 in Supporting Information S1). The $\delta^2\text{H}_{\text{H}_2\text{O}}$ and $\delta^{18}\text{O}_{\text{H}_2\text{O}}$ values spanned from -52.5‰ to -1.0‰ and from -8.1‰ to $+6.4\text{‰}$, respectively (Figure 4a, Table S5 in Supporting Information S1). While eight samples from the Chukuo fault and Coastal Range fell along the local meteoric water line (LMWL, Peng et al., 2010), the others deviated from the LMWL by varying degrees.

5. Discussion

5.1. First Order Assessments on the Origins of Methane

Conventional approaches based on bulk isotopic compositions of methane and CO_2 , and abundance ratios were first used to interpret the origins of hydrocarbon gases for individual structural domains (e.g., Milkov, 2011; Milkov & Etiope, 2018). The principle stems from laboratory and field observations (e.g., Bernard et al., 1977; Milkov & Etiope, 2018; Whiticar, 1999) that thermogenic gases are generally characterized by relatively high $\delta^{13}\text{C}_{\text{CH}_4}$ and $\delta^2\text{H}_{\text{CH}_4}$ values (from -60‰ to -25‰ , and -300‰ to -150‰ , respectively), low C_1/C_2^+ ratios (1–100), and low $\delta^{13}\text{C}_{\text{CO}_2}$ values. Microbial gases possess geochemical characteristics (low $\delta^{13}\text{C}_{\text{CH}_4}$ and $\delta^2\text{H}_{\text{CH}_4}$ values ($<-50\text{‰}$ and $<-150\text{‰}$, respectively; Whiticar, 1999), and high C_1/C_2^+ ratios ($>1,000$, Bernard et al., 1977)) distinct from thermogenic gases by various degrees (even though the less fractionated isotopic compositions of microbial methane resemble early mature thermogenic gases). Abiotic gases may follow variable patterns partially overlapping with thermogenic gases and with a tendency toward greater $\delta^{13}\text{C}_{\text{CH}_4}$ values (Milkov & Etiope, 2018). For comparison, as CO_2 derived from biodegraded oil is converted into secondary microbial methane, the residual CO_2 becomes progressively enriched in ^{13}C (Head et al., 2003). Biodegradation also leads to an increasing CH_4 fraction in the gas. Furthermore, methane oxidation (aerobic and anaerobic styles) and diffusive transport would all lead to the residue methane enriched with ^{13}C and ^2H by various degrees (Figure 1, Whiticar, 1999). Therefore, gas alteration and mixing can complicate possible interpretations.

Based on these empirical fields defined in $\delta^{13}\text{C}$ and $\delta^2\text{H}$ values, and C_1/C_2^+ ratios, 15 out of the 31 samples could be interpreted as dominantly thermogenic in origin (Figure 1, Tables S1 and S2 in Supporting Information S1). While these samples were primarily distributed along the Chukou and Chishan faults, 4 of 15 samples were from

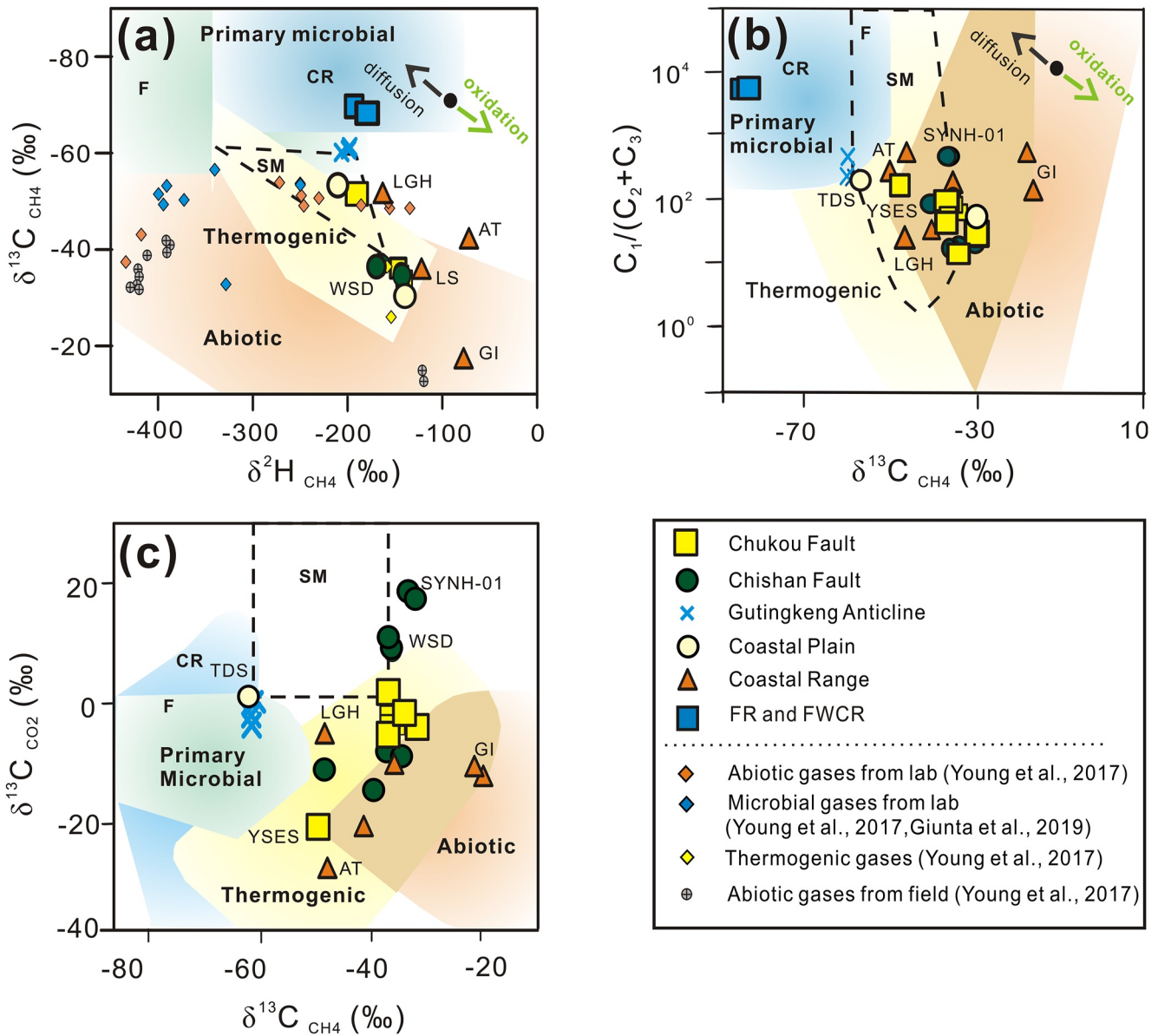


Figure 1. Isotopic and abundance characteristics of hydrocarbons and CO_2 for analyzed samples. (a) $\delta^{13}\text{C}_{\text{CH}_4}$ versus $\delta^2\text{H}_{\text{CH}_4}$ values (data from Table S2 in Supporting Information S1); (b) $C_1/(C_2 + C_3)$ ratios versus $\delta^{13}\text{C}_{\text{CH}_4}$ values (data from Table S1 in Supporting Information S1); (c) $\delta^{13}\text{C}_{\text{CO}_2}$ versus $\delta^{13}\text{C}_{\text{CH}_4}$ values (data from Table S1 in Supporting Information S1). The plotted fields are divided into areas for “primary microbial” (shaded in green and blue), “secondary microbial” (encircled by dashed lines and abbreviated as “SM”), “thermogenic” (shaded in yellow), and “abiotic” (shaded in orange) formation processes following the ranges of Milkov and Etiope (2018). “Primary microbial” methane is further divided into two categories, with “F” for the fermentation of methylated compounds and “CR” for the CO_2 reduction. Results are categorized by structural domains (yellow squares—Chukou Fault, green circles—Chishan Fault, crosses—Gutingkeng Anticline, light yellow circles—Coastal Plain, blue squares—offshore FR, and Four Way Closure Ridge sites, orange triangles—Coastal Range). Green and black arrows in panels (a, b) show the possible trends for microbial methane oxidation and diffusion of migratory methane, respectively. The slope of the arrow does not indicate the precise variation trend. Some published results for different processes simultaneously characterized by the abundances of doubly substituted isotopologues (Giunta et al., 2019; Young et al., 2017) are plotted for comparison.

the Coastal Range (sites LGH and LS), the Gutingkeng anticline (site LCW), and the Coastal Plain (site WD). For comparison, data for two boreholes from the Coastal Range (sites AT and GI) were interpreted as abiotic in origin (Figure 1). On the Bernard plot (Figure 1b), these data points fell either within the empirically defined abiotic field or the overlapping range between the thermogenic and abiotic fields (Milkov & Etiope, 2018). The $\delta^2\text{H}_{\text{CH}_4}$ values for both sites (between -79‰ and -77‰) and the $\delta^{13}\text{C}_{\text{CH}_4}$ value for site GI were much higher than those commonly identified as thermogenic methane. This, combined with their high temperature nature, proximity

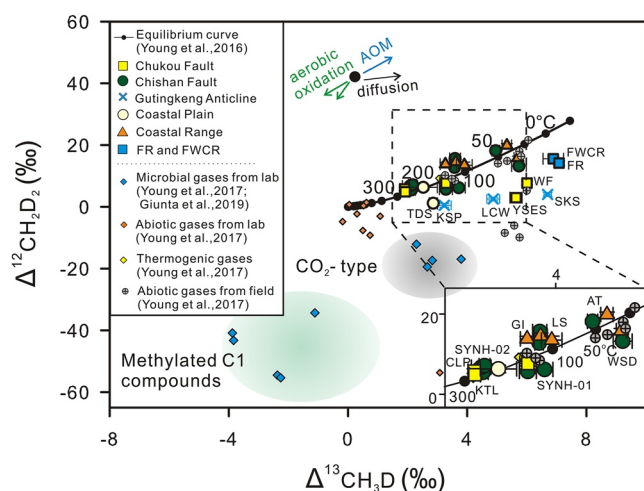


Figure 2. $\Delta^{12}\text{CH}_2\text{D}_2$ versus $\Delta^{13}\text{CH}_3\text{D}$ values for analyzed samples. The equilibrium curve marked with temperature was calculated following Young et al. (2016). Sample legends are the same as those in Figure 1. Values for microbial methane produced from methylated compounds and from CO_2 in the lab (blue diamonds encompassed with an arbitrarily defined range in green and gray, Giunta et al., 2019; Young et al., 2017) and abiotic methane produced in the laboratory (orange diamonds) or recovered from the field (gray circles with cross marks) (Young et al., 2017) are plotted for comparison. Green, black, and blue arrows show the possible trends for aerobic oxidation of methane, diffusion of migratory methane, and anaerobic oxidation of methane, respectively. The slope of the arrow does not indicate the precise variation trend. Data distribution within the region encircled by a dashed rectangle is enlarged in the lower right corner.

to the volcanic bodies, and island arc setting, suggests that methane could be abiotic (Milkov, 2011; Milkov & Etiope, 2018). Data for two marine sediments (sites FR and FWCR) were categorized as microbial in origin, whereas data points for LGH (Coastal Range), TDS (Coastal Plain), YSES (Chukou fault), and all samples from the Gutingkeng anticline fell between typical ranges of thermogenic and microbial end components (Figure 1b, see Section 5.3 for the mixing model).

The $\delta^{13}\text{C}_{\text{CO}_2}$ values of samples collected from the Chishan fault fell between -15.9‰ and $+20.5\text{‰}$ (Figure 1c, Table S1 in Supporting Information S1). In particular, $\delta^{13}\text{C}$ values of CO_2 and DIC for SYNH-01, and WSD -01 and -02 ranged from $+8.9\text{‰}$ to $+20.5\text{‰}$ and from $+18.5\text{‰}$ to $+30.6\text{‰}$, respectively. This, combined with the detection of active CO_2 reducing methanogens in the region (Cheng et al., 2012; Y. T. Lin et al., 2018), suggests that the ^{13}C enrichment in CO_2 is catalyzed by secondary methane formation from CO_2 . Secondary microbial methane is formed through the anaerobic degradation of petroleum (Head et al., 2003). As CO_2 is the byproduct of petroleum degradation, its quantity is limited by the degradability of petroleum, and therefore, it is considered as a close system. In this regard, further methane formation would preferentially reduce $^{12}\text{CO}_2$ over $^{13}\text{CO}_2$, leaving the residue CO_2 enriched with ^{13}C and methane depleted in ^{13}C . The interpretation is also supported by the presence of patchy oils constantly observed in the bubbling pools or craters. To assess this process, a Rayleigh distillation model was applied assuming an initial $\delta^{13}\text{C}_{\text{DIC}}$ value of -25‰ and a fractionation factor ($\alpha_{\text{DIC-CH}_4}$) of 1.05 (Chasar et al., 2000). The calculation also assumed that CO_2 or DIC in environments was produced primarily from the degradation of organic matter with $\delta^{13}\text{C}$ values between -30‰ and -20‰ (Campeau et al., 2017). Since the isotopic fractionation for organic degradation is small ($<1\text{‰}$), the median $\delta^{13}\text{C}$ value (-25‰) was arbitrarily chosen

for modeling. The calculation suggests that in order to replicate the observed $\delta^{13}\text{C}_{\text{DIC}}$ value, the fraction of the reaction would be 36% or the concentration of DIC consumed or methane produced would be equivalent to 57 mM. The quantity of DIC reduced or methane produced is at least one order of magnitude higher than the observed maximum methane concentration (2 mM). If the fractionation factor is raised to a more extreme level of 1.08 (Summons et al., 1998), the reaction fraction would reach 54%, or the concentration of methane produced would be 34 mM. The overall results from the Rayleigh distillation modeling suggest that secondary methane

formation by CO_2 reducing methanogens might not be solely responsible for the ^{13}C enrichment in CO_2 or DIC. Other microbial channels, such as acetate formation from CO_2 (Karakashev et al., 2006), might be involved. Alternatively, the high predicted concentration of methane could have been lost due to the depressurized degassing during transport along the fluid conduit. The temperature of methane formation for SYNH has been estimated to be up to 236°C (Figure 2, Table S2 in Supporting Information S1). By applying a local geothermal gradient of $25^\circ\text{C}/\text{km}$ (Chi & Reed, 2008), the formation depth could range up to 9 km below the land surface. As methane ascends toward the land surface, dissolved methane is depressurized and transformed into bubbles. The inference is supported by vigorous bubbling at SYNH during sampling.

Excess methane or carbon could not be accounted for by the anabolic assimilation as most substrate consumptions are often diverted to the energy yield rather than biosynthesis. For example, tests on *S. fumaroxidans* cocultured with *M. hungate* have obtained a yield of 0.15–0.25 mol- $\text{CH}_4/\text{g-dw-biomass}$ (Scholten & Conrad, 2000). If 50% of biomass is attributed to carbon, the yield would range from 3.57 to 5.95 mol- $\text{CH}_4/\text{mol-C-biomass}$. For every mole of CO_2 utilized, less than 20% of it is diverted to biomass generation. Even

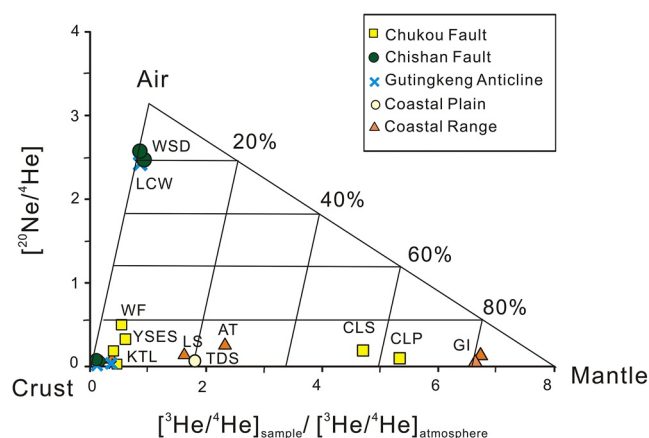


Figure 3. $^{20}\text{Ne}/^4\text{He}$ versus $^3\text{He}/^4\text{He}$ ratios (in Ra) for analyzed samples. A three end-component mixing model encompasses “crust,” “mantle,” and “air” components with He isotope ratios of 0.01, 8, and 1 Ra, respectively (Poreda & Craig, 1989). Legends are the same as those in Figure 1.

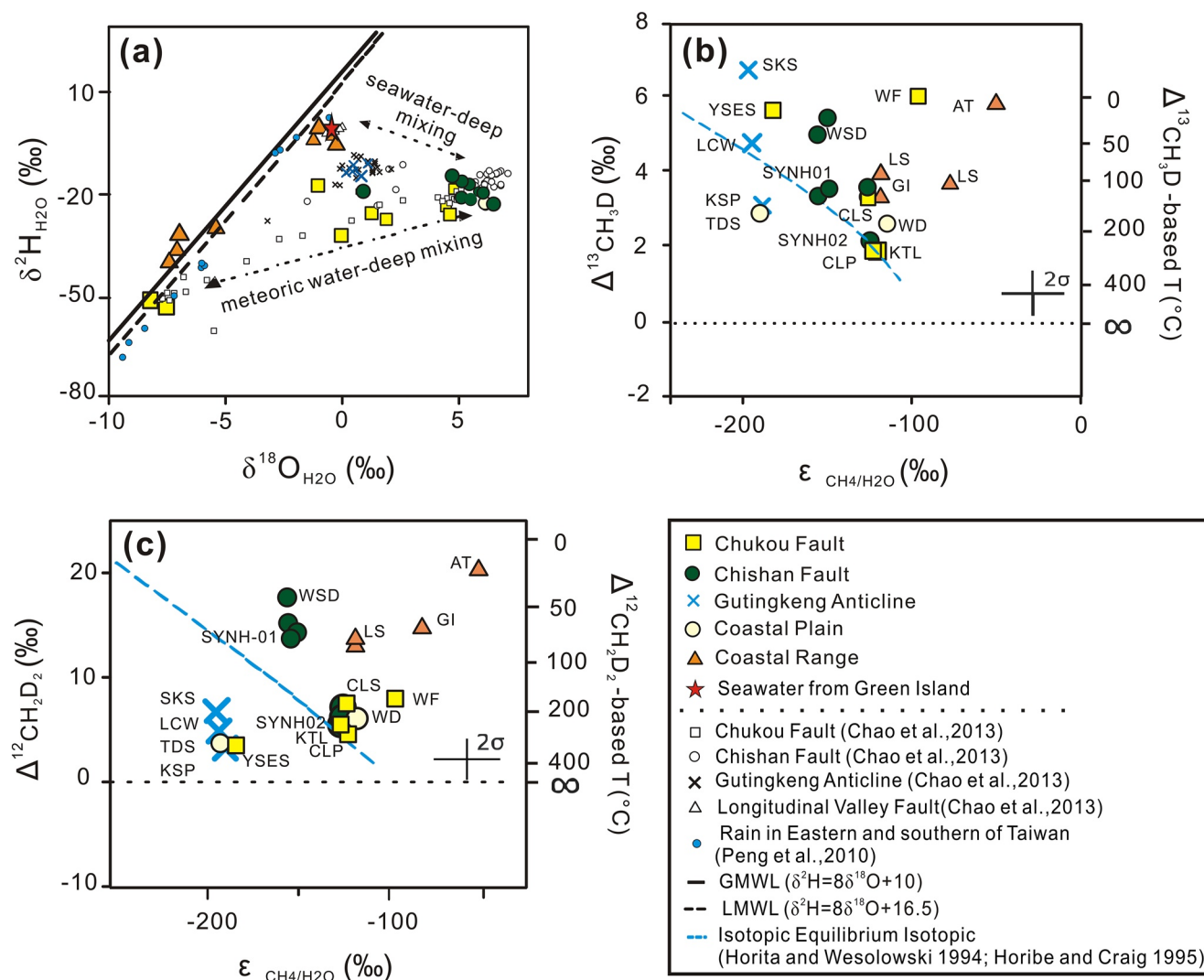


Figure 4. Water isotopic compositions and fractionations, and methane isotopologue abundances. (a) Water $\delta^2\text{H}$ versus $\delta^{18}\text{O}$ values for analyzed samples. Legends are the same as those in Figure 1 (except for the red star for seawater from the Green Island; small blue circles for meteoric water in eastern and southern Taiwan). The solid line indicates the global meteoric water line (Craig, 1961), whereas the dashed line is the local meteoric water line (Peng et al., 2010). The dotted lines with arrows indicate the potential mixing between deeply sourced water and meteoric water or seawater. Data for mud volcanoes published in previous studies are also plotted for comparison. (b) $\Delta^{13}\text{CH}_3\text{D}$ and (c) $\Delta^{12}\text{CH}_2\text{D}_2$ values versus hydrogen isotopic fractionations (ϵ ; defined as $(\alpha - 1) \times 1,000\%$, where α is the fractionation factor (Equation 8) between methane and water). The equilibrium curves (in blue dashed lines) are plotted using the relationships described in Horita and Wesolowski (1994) and Horibe and Craig (1995). The dotted lines indicate an infinite temperature that is based on two methane isotopologue abundances (Young et al., 2016).

with this, the predicted CO_2 consumption or CH_4 production still greatly exceeds the observed methane concentrations. In sum, the bulk isotopic compositions provide a first-order interpretation of the origin of hydrocarbons (methane in particular). While the excess methane predicted for the Chishan fault could have been accounted for by the depressurization loss, the interpretation of the origins of all samples is still subject to variations caused by potential mixing with a small fraction of non-major end components.

The majority of $\Delta^{13}\text{CH}_3\text{D}$ and $\Delta^{12}\text{CH}_2\text{D}_2$ values for samples from the Chukou and Chishan faults, and the Coastal Range were distributed either on, or close to the equilibrium curve (Figure 2). The equilibrium temperatures were calculated to range from 23° to 260°C for sites CLP, CLS, and KTL in the Chukou fault, sites WSD-01 and SYNH-02 in the Chishan fault, site WD in the Coastal Plain, and sites AT and LS in the Coastal Range (Table S2 in Supporting Information S1). Except for sites WSD-01 and AT, samples that displayed the isotopologue equilibrium also possessed bulk isotopic compositions and abundances interpreted as the products of thermal maturation of organic matters at high temperatures. Such a pattern is comparable with the observations

of large-scale continental sedimentary basins, the Southwest Ontario and the Michigan Basin, as described by Giunta et al. (2019). Although the $\Delta^{13}\text{CH}_3\text{D}$ and $\Delta^{12}\text{CH}_2\text{D}_2$ values for sites WSD-01 and AT yielded comparable temperature estimates, these isotopologue abundances were considered to represent either a mixture of thermogenic and microbial (for site WSD-01) sources, or abiogenic methane (for site AT) (see Sections 5.3 and 5.4).

5.2. Re-Equilibration and Other Secondary Processes for Methane

Post-formation secondary mechanisms, including re-equilibration, microbial methane oxidation, and diffusive transport, have been proposed to explain the variations in clumped isotope composition that do not align well with the thermodynamic equilibrium (Beaudry et al., 2021; Giunta et al., 2021, 2022; Jautzy et al., 2021; Krause et al., 2022; Labidi et al., 2020b; J. Liu et al., 2023; Ono et al., 2021; Shuai et al., 2018; Stolper et al., 2015; Young et al., 2017). Re-equilibration is referred to the process that alters the original clumped isotopic compositions toward or along the thermodynamic equilibrium at a temperature range or condition either comparable with or drastically different from the current in situ setting. Because the re-equilibration takes place with intra-molecular re-ordering, the bulk isotopic compositions could have remained unaltered (Giunta et al., 2021; Labidi et al., 2020b). The mechanism has been used to account for the origins of methane from the Precambrian continental shield, hydrothermal systems, Baltic Sea sediments, and seep sediments from the Marmara Sea (Ash et al., 2019; Giunta et al., 2021; Labidi et al., 2020b). The interpretation becomes even more appealing when the bulk isotopic compositions are apparently kinetic controlled (e.g., microbial methanogenesis) and clumped isotopic compositions reflect a state of or close to the thermodynamic equilibrium (Ash et al., 2019; Giunta et al., 2022; Ono et al., 2021).

To assess this inference, the probability of data distribution for $\Delta^{13}\text{CH}_3\text{D}$ and $\Delta^{12}\text{CH}_2\text{D}_2$ values for mud volcanoes in western Taiwan and offshore sediments were plotted considering their structural configuration and hosted formations might resemble each other (Figure S4 in Supporting Information S1). Like that reported by Giunta et al. (2021), the $\Delta^{13}\text{CH}_3\text{D}$ values were scattered across the measured range and did not exhibit any pattern that demonstrated the clustering within a particular interval. In contrast, the $\Delta^{12}\text{CH}_2\text{D}_2$ values clustered within two broad ranges (0‰–8‰ and 12‰–17‰) if a 1‰ interval was chosen. The bi-modal data distribution became even more prominent if a 2‰ interval was used (Figure S4 in Supporting Information S1). The re-equilibration hypothesis lies on the premise that the intra-molecular re-ordering of $^{12}\text{CH}_2\text{D}_2$ proceeds at a rate much faster (probably 2 times higher) than $^{13}\text{CH}_3\text{D}$. Therefore, over the course of re-equilibration, $\Delta^{13}\text{CH}_3\text{D}$ values produced by kinetic reactions (e.g., methanogenesis or thermal maturation) would vary toward the equilibrium line while $\Delta^{12}\text{CH}_2\text{D}_2$ values remain at a relatively invariant range. Under this circumstance, the estimated temperature projected by clustering $\Delta^{12}\text{CH}_2\text{D}_2$ values could be used to infer the possible temperature of re-equilibration, whereas $\Delta^{13}\text{CH}_3\text{D}$ values represent the degrees of partial re-equilibration. The inference of re-equilibration described above is not favored based on the following arguments.

1. The two clusters of $\Delta^{12}\text{CH}_2\text{D}_2$ values obtained in this study could be translated into the estimated temperatures of $60^\circ \pm 10^\circ\text{C}$ and $200^\circ \pm 50^\circ\text{C}$ (Figure S4b in Supporting Information S1). The lower one ($60^\circ \pm 10^\circ\text{C}$) is derived from the samples collected from the Chishan fault (SYNH-01 and WSD) and offshore sediments. All samples from the Chishan fault possess bulk isotopic compositions interpreted as thermogenic methane, and $\Delta^{13}\text{CH}_3\text{D}$ and $\Delta^{12}\text{CH}_2\text{D}_2$ values close to the equilibrium curve. For comparison, bulk isotopic compositions of methane in marine sediments indicate typical microbial origin. If the hypothetical re-equilibration proceeds with the variation in $\Delta^{13}\text{CH}_3\text{D}$ value only, the re-equilibration would occur at a temperature ($60^\circ \pm 10^\circ\text{C}$), which is lower than the gas window commonly considered for the formation of thermogenic methane ($>80^\circ\text{C}$) (Pepper & Corvi, 1995). The scenario is unlikely unless the catalyst involved in the re-equilibration is sufficiently efficient to facilitate the intra-molecular re-ordering of methane isotopologues at that low temperature. Instead, the data distribution (both bulk isotopic and clumped compositions) could be best explained by the mixing between a thermogenic end component and a microbial end component represented by the offshore sediments (Figure S5 in Supporting Information S1, see Section 5.3 for details).
2. The cluster with higher projected temperatures ($200^\circ \pm 50^\circ\text{C}$) (Figure S4b in Supporting Information S1) encompasses several sub-clusters spanning over 30‰ of $\Delta^{12}\text{CH}_2\text{D}_2$ values. Values off the equilibrium line were derived from samples collected from the Chukou fault, Chishan fault, Gutingkeng anticline, and Coastal Plain. For samples from the Chukou and Chishan faults, the majority of their $\delta^{13}\text{C}$ and $\delta^2\text{H}$ values are interpreted as thermogenic in origin (with the exception of YSES). For comparison, all samples from the Gutingkeng

anticline and Coastal Plain possessed $\delta^{13}\text{C}$ and $\delta^2\text{H}$ values categorized as a mixture of microbial and thermogenic origins. By examining the details, the projected temperatures of re-equilibration based on $\Delta^{12}\text{CH}_2\text{D}_2$ values range around 200°C and could reach as high as 686°C (Table S2 in Supporting Information S1). If the former projected temperature represents a temperature of re-equilibration, the re-equilibration would proceed with a burial of approximately 7 km depth (assuming the geothermal gradient is $25^\circ\text{C}/\text{km}$, Chi & Reed, 2008) following the initial formation through either a microbial process or thermal maturation. Since the disequilibrium clumped isotopic composition for thermogenic methane has not been affirmatively validated for environmental samples (Shuai et al., 2018; Xia & Gao, 2019), only the scenario for the re-equilibration of microbial methane is addressed here. Although the temperature limit to life or methanogenesis could range up to 122°C (Takai et al., 2008), the formation of microbial methane in petroleum or natural gas systems is generally considered to take place at temperatures less than 80°C (Head et al., 2003). In this regard, at least additional ~ 5 km of burial after its initial formation is presumably needed to reach the temperature for the designated re-equilibration. To assess this possibility, the uplift history of Taiwan orogenesis that has accommodated the shortening between the Luzon arc and the Eurasian plate is utilized. While the collision started at about 5 Ma (based on the first appearance of slate fragments in the sedimentary records; Teng, 1987), the uplift and exhumation accelerated during the period of 1–2 Ma (T. W. Chen et al., 2023; Lee et al., 2022). If an uplift rate of 1 cm/yr is assumed (T. W. Chen et al., 2023; Yen et al., 2008), a total of 1,000–2,000 m of uplift would be expected. The estimate does not take erosion (up to 5 mm/yr based on ^{10}Be dating, Fellin et al., 2017) into account and should be considered an optimum scenario. This quantity could also be translated into the burial of the formations in the footwall of thrust faults. Unless the uplift rate could be raised by at least a factor of 2.5 and the erosion could be ignored, the estimated optimum burial is apparently not sufficient to reach the designated re-equilibration temperature.

- Some of the data points for the high temperature cluster were distributed at $\Delta^{12}\text{CH}_2\text{D}_2$ values of less than 4 (samples collected from the Chukou fault, Gutingkeng anticline, and Coastal Plain). If these data points are attributed to the hypothetical re-equilibration, then the re-equilibration temperatures could be at least 261°C and reach as high as 686°C (Table S2 in Supporting Information S1). Such a temperature range requires an unlikely burial depth as described and exceeds the upper bound for thermal maturation. Again, the data distribution could not be accounted for by re-equilibration.

For microbial methane oxidation, bulk isotope compositions for residue methane would generally increase with the extent of consumption (Whiticar, 1999). Depending on the fractionation factors, the enrichment in heavier isotopes would vary considerably among species or environmental characteristics. In contrast, the clumped isotopic compositions exhibit drastically different patterns between aerobic and anaerobic methane oxidation based on culture, enrichment, and environmental observations. The $\Delta^{13}\text{CH}_3\text{D}$ and $\Delta^{12}\text{CH}_2\text{D}_2$ values either decrease off or along the equilibrium curve for aerobic methane oxidation (Giunta et al., 2022; Krause et al., 2022), or cluster close to or along the equilibrium curve and its extension off 0°C mark or vary off the equilibrium curve and along the $\Delta^{12}\text{CH}_2\text{D}_2$ axis for anaerobic oxidation of methane (AOM) (Ash et al., 2019; Giunta et al., 2022; J. Liu et al., 2023; Ono et al., 2021). In one case for the Baltic Sea sediments (Ash et al., 2019), a methanogenic zone is sandwiched by two sulfate-methane transition zones (SMTZ) attributed to the sulfate- and Fe-AOM. The $\Delta^{13}\text{CH}_3\text{D}$ and $\Delta^{12}\text{CH}_2\text{D}_2$ values for the deep SMTZ are nearly constant, reaching a thermodynamic equilibrium at a temperature consistent with the in situ 7.8°C . The results obtained from the Black Sea sediments, on the other hand, exhibit a different pattern (Giunta et al., 2022). Their $\Delta^{13}\text{CH}_3\text{D}$ and $\Delta^{12}\text{CH}_2\text{D}_2$ values are close to the equilibrium curve at the bottom of SMTZ and increase to a highly enriched level (15‰ – 16‰ for $\Delta^{13}\text{CH}_3\text{D}$ and 60‰ – 75‰ for $\Delta^{12}\text{CH}_2\text{D}_2$) at the top of the SMTZ, a pattern also observed in the incubations of AOM enrichment from Svalbard sediments (J. Liu et al., 2023). For comparison, the potential AOM in seep sediments (from Santa Barbara Channel) and deep materials (Nankai sediments and Beatrix fluids) shift the $\Delta^{13}\text{CH}_3\text{D}$ value toward the thermodynamic equilibrium with an insignificant change in $\Delta^{12}\text{CH}_2\text{D}_2$ value (J. Liu et al., 2023). The contrast patterns of isotopologue abundances have been linked to the reversibility of methane oxidation potentially controlled by the thermodynamic drive intrinsically linked to the availability of sulfate and methane (J. Liu et al., 2023; Ono et al., 2021, 2022). For the abundant substrate (and energy flow) like that attested by culture experiments, AOM is regulated by kinetic effects that lead to the disequilibrium isotopologue abundances. In contrast, AOM imposed by limited substrate availability proceeds with the high reversibility so that thermodynamic equilibrium could be readily reached. Various thresholds of the substrate availability have been proposed primarily based on field observations (Ash et al., 2019; Giunta et al., 2022; Ono et al., 2021), thereby warranting the validation from laboratory tests.

To address the potential of AOM for this study, the distribution of $\Delta^{13}\text{CH}_3\text{D}$ and $\Delta^{12}\text{CH}_2\text{D}_2$ values was first examined. Only two seep sediments (FWCR and FR) possess $\Delta^{13}\text{CH}_3\text{D}$ and $\Delta^{12}\text{CH}_2\text{D}_2$ values resembling those from the Baltic and Black Seas near the equilibrium curve at the lower temperature end. However, these two sediments were retrieved from the gas hydrate stability zone at a depth of 108 m for FWCR and 22 m for FR below the seafloor. Based on the geochemical characteristics (Bohrmann et al., 2023), these samples are not representative of sediments typical for AOM. Furthermore, the data points for mud volcanoes in western Taiwan (Figure S4 in Supporting Information S1) are not near the lower temperature end of the equilibrium line but resemble the shift caused by potential AOM that proceeds with high reversibility under or near thermodynamic threshold (J. Liu et al., 2023). Although sulfate-AOM at <10 cm depth has been validated based on the geochemical profile and genetic data for SYNH (Cheng et al., 2012; Y. T. Lin et al., 2018), these samples were collected from the mud platform formed by the accumulation of fluidic mud emanating from the bubbling pool. Here, sulfate-AOM is fueled by methane percolating off the major fluid conduit and through the porous medium, and by sulfate generated by the oxidation of pyrite or iron sulfide through the exposure of deeply sourced sediments to the atmosphere. As our samples were collected from the bubbling pools that represent the surface expression of subsurface fluid channels, collected gases were plumbed from the deep source with minimum alteration during the transport, thereby exhibiting geochemical and community composition patterns distinct from those in the mud platform. Similarly, aerobic methane oxidation has been validated with geochemical, incubation, and genetic data for the mud platform sediments at SYNH (Cheng et al., 2012; Y. T. Lin et al., 2018). Again, companion data for samples collected from bubbling pools are distinct from those from the mud platform. The bulk and clumped isotopic compositions for our samples were also not aligned with the ranges commonly attributed to aerobic methane oxidation (Figures 2 and 3). Taken together, while these lines of evidence do not favor microbial methane oxidation (either anaerobic or aerobic style) as the main cause of isotopic variations, the possibility of AOM could not be completely ruled out.

Finally, molecular diffusion has been considered to address the isotopic variations (both bulk and clump isotopes) (Giunta et al., 2021). The tenuous nature of the diffusive pathway in sedimentary rocks would particularly enable the mass-differentiation transport during fluid percolation over a long-distance range. According to the rules of mass difference (Etiope, 2009), diffusion facilitates to transport lighter isotopes over heavier ones, resulting in the preferential depletion of ^{13}C or smaller $\delta^{13}\text{C}/\delta^2\text{H}$ values for migratory methane (or vice versa for residue methane). On the other hand, the corresponding $\Delta^{12}\text{CH}_2\text{D}_2$ versus $\Delta^{13}\text{CH}_3\text{D}$ values would increase (Giunta et al., 2021). Both these variation trends follow a 1:1 slope in the $\delta^2\text{H}$ versus $\delta^{13}\text{C}$ and $\Delta^{12}\text{CH}_2\text{D}_2$ versus $\Delta^{13}\text{CH}_3\text{D}$ plots (Figure S4 in Supporting Information S1; constrained by the beta value (0.05) for single or double substituted isotopologues). Either plot for the data reported in this study reveals that diffusion seems to account for multiple linear distributions of isotopic compositions (Figure S4 in Supporting Information S1). However, if a $\delta^{13}\text{C}$ value of -33‰ (CLP; thermogenic methane) is used to anchor one end of the diffusion trend in the plot of $\Delta^{13}\text{CH}_3\text{D}$ versus $\delta^{13}\text{C}$ (Figure S4 in Supporting Information S1), it is apparent that the variations in $\delta^{13}\text{C}$ value is not sufficient to account for those in $\Delta^{13}\text{CH}_3\text{D}$ value (nearly all data points plotted above the diffusion trend). If diffusion is the governing mechanism for isotopic fractionation, the anchor point in $\delta^{13}\text{C}$ axis has to be set at a higher value ($>-20\text{‰}$), a scenario more likely representing abiotic source and not supported by the current data. Again, diffusion could not explain the data variation.

Overall, the data pattern, the geological context, and the projected temperature based on individual isotopologue abundance are not in favor of the re-equilibration, microbial methane oxidation, and diffusive transport as a broad-scaled control on the variations in bulk and clumped isotopic compositions. For those clumped isotopic compositions off the equilibrium line, the mixing between thermogenic and microbial sources appears to be the most plausible explanation for most samples (see Section 5.3 for details). Since these samples are distributed in several structural domains, the exchange of fluids and gases between domains is unlikely. Lumping all data together across structural domains could have potentially masked the intrinsic characteristics associated with primary and secondary mechanisms responsible for the formation or alteration of methane for individual structural domains or samples. To unequivocally discern methane origins in such a tectonically complex and fragmented terrain as Taiwan, a wider coverage of sampling with designated targets and designed laboratory experiments is warranted.

5.3. Mixing of Methane, Helium, and Nitrogen Between Sources

The isotopologue abundances provide an extra dimension to account for a mixed origin, in addition to bulk isotopic compositions and abundance ratios. The mixing scenarios are discussed here in accordance with the structural

domains. As the exact mechanisms and characteristics of abiogenic methane are still vague, the mixing scenarios are limited to using thermogenic and microbial end components. In principle, the highest estimated temperatures based on isotopologue abundances for the individual structural domain were selected as the thermogenic end component. Results obtained from culture experiments (Giunta et al., 2019; Young et al., 2017) were first used as the microbial end component. Other than that, environmental samples indisputably attributed to methanogenesis could also be considered. To avoid arbitrary designation, it would be even better if the target samples and environmental samples treated as the end component could belong to a similar/same geological context. Therefore, the potential heterogeneity of the end component compositions would be taken into account. Regardless of which end component is chosen, the mixing scenarios based on bulk and clumped isotopic compositions should be coherent. For sites along the Chishan fault, methane from some sites (SYNH-01 and WSD-01) was partially produced by secondary CO₂ reduction (see Section 5.1). Their bulk isotopic compositions slightly deviated from the potential end component of thermal maturation ascribed to SYNH-02. To quantify the contribution of thermogenic versus microbial methane, mass conservation was first applied with a thermogenic end component represented by $\delta^{13}\text{C}_{\text{CH}_4}$ of -35.3‰ and $\delta^2\text{H}_{\text{CH}_4}$ of -143.6‰ (site SYNH-02), and a microbial end component represented by average culture values for either CO₂ reduction methanogenesis ($\delta^{13}\text{C}_{\text{CH}_4}$ of -51.1‰ and $\delta^2\text{H}_{\text{CH}_4}$ of -389.4‰) or methylotrophic methanogenesis ($\delta^{13}\text{C}_{\text{CH}_4}$ of -45.8‰ and $\delta^2\text{H}_{\text{CH}_4}$ of -299.4‰) (Giunta et al., 2019; Young et al., 2017). For sites SYNH-01 and WSD-01, their similar bulk isotopic compositions both yielded 10% and 25% contributions of microbial methane from CO₂ and methylated compounds, respectively (Figure S5 in Supporting Information S1). Similar approaches were adopted in the isotopologue mixing model ($\Delta^{13}\text{CH}_3\text{D}$ of 2.13‰ and $\Delta^{12}\text{CH}_2\text{D}_2$ of 5.47‰ from site SYNH-02 for the thermogenic end component; $\Delta^{13}\text{CH}_3\text{D}$ of 2.90‰ and $\Delta^{12}\text{CH}_2\text{D}_2$ of -16.46‰ from methanogens in laboratory (Giunta et al., 2019; Young et al., 2017) as the average microbial end component). The calculation yielded a 60% microbial fraction for site SYNH-01, and 45% for site WSD-01 from CO₂ reduction methanogenesis (Figure S5 in Supporting Information S1). For comparison, the isotopologue mixing model based on methylotrophic methanogenesis could not replicate the observations.

Marine sediments collected offshore Taiwan (FR and FWCR) as the potential microbial end components were also assessed. These two samples possessed bulk isotopic compositions typical for microbial methane ($\delta^{13}\text{C}_{\text{CH}_4}$ of -69‰ and $\delta^2\text{H}_{\text{CH}_4}$ of -190‰). Their clumped isotopic compositions were, however, distinct from the culture representatives, and distributed off the equilibrium line (Figure 2) in the space occupied with a number of data points from marine sediments (Ash et al., 2019; Giunta et al., 2022). The mixing scenarios are not coherent between clumped and bulk isotopic compositions. While the isotopologue mixing model yielded a microbial contribution ranging from 20% to 60%; (Figure S5 in Supporting Information S1), the bulk-based mixing model yielded a much less microbial contribution (<10%) with greater uncertainties.

For sites in the Chukou fault, the Gutingkeng anticline, and the Coastal Range, a mixing model was constructed using a similar thermogenic end component (KTL for the Chukou fault, SYNH-02 for the Gutingkeng anticline, and LS for the Coastal Range) and a microbial end component derived from marine sediments (either FR/FWCR values or $\delta^2\text{H}_{\text{CH}_4}$ and $\Delta^{12}\text{CH}_2\text{D}_2$ values slightly smaller than FR/FWCR values). The calculations for bulk isotopic and isotopologue mixing yielded comparable fractions (40%–80% for bulk isotope mixing and 20%–90% for isotopologue mixing) of the microbial end component (Figure S5 in Supporting Information S1), a pattern consistent with the detection of methanogens using different substrates in these regions (Y. H. Chang et al., 2012; Ling et al., 2012; P. L. Wang et al., 2014).

Helium isotopic ratios ranged from 0.1 to 6.8 Ra (Figure 3, Table S4 in Supporting Information S1). Most ratios (except for sites AT, CLP, CLS, TDS, GI, and LS) were smaller than 1 Ra, indicating that the gases originated from a crustal component. The N₂ isotopologue results appear to be correlated with helium isotopes. Three sites (KTL-02, WSD-01, and AT) showed Δ_{30} values ranging between +11‰ and +17‰ (Figure S3 and Table S3 in Supporting Information S1). This is lower than the air value of +19.3‰ (Yeung et al., 2017) but much higher than 0‰ observed for crustal and volcanic nitrogen (Labidi et al., 2020a), suggesting the addition of the air to deep crustal/volcanic nitrogen. A mass balance calculation yielded that 40%–80% of the N₂ in the gas mixtures must be accounted for by the air-derived nitrogen. In other words, the nitrogen with a deep origin with a Δ_{30} value of 0‰ (Labidi et al., 2020a) contributed to 20%–60% of the gas mixtures. While no robust $\delta^{15}\text{N}$ estimate could be provided for the crustal nitrogen end component, $\delta^{15}\text{N}$ values tend to vary toward a more negative range (-2.1‰) for the samples with the highest air contributions. This likely reflects mass-dependent fractionation of atmospheric nitrogen in the subsurface (Labidi & Young, 2022) rather than a signature from deep nitrogen. The Δ_{30} pattern for KTL and WSD in the Western Foothills is consistent with crustal helium signatures and

methane formations at temperatures of 260°C (for KTL). However, the deep nitrogen source for AT in the Coastal Range is not necessarily only the crustal component. Its $^3\text{He}/^4\text{He}$ ratio is relatively high (2.3 Ra), suggesting a mixture between the mantle and air/crust. The bulk and clumped isotopic compositions of methane are interpreted as the abiotic origin with the formation temperature or depth unconstrained (see Sections 5.1 and 5.4 for details). If nitrogen shares the same source of helium, the deep source is at least partially composed of the mantle component. For comparison, the two GI duplicates with 6.7 Ra and 6.8 Ra showed Δ_{30} values of 3.1‰ and 1.8‰, a range close to 0‰. This likely reflects marginal (<10%) air contributions. Their $\delta^{15}\text{N}$ values were +3.6‰, a pattern consistent with the signature associated with subducted nitrogen, which is later accumulated in sub-arc mantle sources worldwide (Busigny et al., 2011; Epstein et al., 2021; Labidi et al., 2021), and previously hypothesized to contribute nitrogen to surface vents in Taiwan (Rouilleau et al., 2015). Together with mantle-derived helium, the recycled nitrogen must have been remobilized toward the surface via volcanism followed by hydrothermal interactions.

While the origins of methane from sites CLP, CLS, TDS, and LS could be constrained by bulk isotopic and isotopologue compositions, and abundance ratios (thermogenic for sites CLP, CLS, and LS, and microbial for site TDS), their anomalous helium isotopic compositions deserve special attention. The analyses yielded $^3\text{He}/^4\text{He}$ ratios that ranged from 1.8 (TDS and LS) to 5.4 Ra (CLP and CLS) and were comparable with data reported previously for sites CLP, CLS (Fu et al., 2021), and LS (Yang et al., 2003). The values suggest a mixture between crustal (0.01 Ra) and mantle components (>8 Ra) (Poreda & Craig, 1989). Except for site LS, the involvement of a mantle contribution is intriguing since the other three sites are all part of the accretionary prism with sporadic volcanism that dates back to 17 Ma and is potentially associated with the opening of the South China Sea (W. S. Chen, 2016). These igneous rocks in the subsurface might account for the continuous degassing of helium with mantle signatures. Alternatively, the supply of helium with mantle signatures could have been along the fault or fracture network extending to the mantle depth. In this regard, helium with mantle signatures should have pervasively infiltrated into the fracture systems of the accretionary prism and been observed at a regional scale, which is not the case in this study. For site LS, the impingement of the Luzon Arc on the Eurasian continent has emplaced numerous igneous bodies in the Coastal Range. Similar to what has been observed for site GI, helium with mantle signatures could have originated from the igneous intrusion in the subsurface. Regardless of the source region, methane and hydrocarbons from igneous bodies are generally considered to possess abiotic signatures, which were not observed for sites associated with sedimentary formations (CLP, CLS, TDS, and LS) but were consistent with the arc setting for sites AT and GI.

Overall, the origins of methane, helium, and nitrogen gases could have been segregated into different compartments of the subduction system. Therefore, their individual mixing patterns would not be necessarily coupled but rather reflect the complexity of sources, transport paths, and fracture connectivity in the tectonically fragmented terrain of Taiwan.

5.4. Potential Abiogenic Methane in the Coastal Range

The methane recovered from sites AT and GI is interpreted as originating from abiotic Fischer-Tropsch Type processes. Their $\Delta^{13}\text{CH}_3\text{D}$ and $\Delta^{12}\text{CH}_2\text{D}_2$ values (Figure 2) overlap with the range for abiotic methane reported in previous studies (Young et al., 2017) and are distributed near (for site GI) or on the equilibrium line (for site AT; corresponding to $\sim 23^\circ\text{C}$) (Figure 2). Laboratory constraints have shown that such surface catalyzed reactions between hydrogen and CO or CO_2 on different metal sulfides proceed at temperatures between 70° and 600°C (Etiope & Lollar, 2013). Field observations and interpretations that combined bulk isotopic compositions, abundance ratios, and water/geological characteristics for regions with prevalent serpentinization have further extended the possible temperature to between 50° and 500°C (Etiope & Lollar, 2013). Limited experiments, however, have shown that methane synthesized from the Sabatier reactions catalyzed by Ru at 70°–600°C yielded $\Delta^{13}\text{CH}_3\text{D}$ and $\Delta^{12}\text{CH}_2\text{D}_2$ values either at the high temperature end of the equilibrium line (>400°C) or distributed over a wide range below the equilibrium line ($\Delta^{13}\text{CH}_3\text{D}$ between 0‰ and +4.5‰ and $\Delta^{12}\text{CH}_2\text{D}_2$ between –55‰ and 0‰) (Young et al., 2017). For comparison, $\Delta^{13}\text{CH}_3\text{D}$ and $\Delta^{12}\text{CH}_2\text{D}_2$ values for Chimaera and Kidd Creek samples attributed to abiotic origin are distributed either along the segment of the equilibrium line between 25° and 150°C or below the equilibrium line (Young et al., 2017). The data pattern obtained in this study is distinct from the experimental constraints but resembles the field observations. However, the temperature estimate based on isotopologue abundances is much lower than the field observation for site AT (23° vs. 62°C).

Such temperature contradiction suggests that both isotopologues do not reach internal equilibrium and thus do not record a true formation temperature. In addition, helium isotopic compositions for sites GI and AT were 6.7 and 2.4 Ra, respectively (Table S4 in Supporting Information S1). This range of helium isotope compositions suggests a higher mantle fraction and is comparable with the proximity to igneous bodies associated with the arc impingement. Overall, the close resemblance of isotopologue abundances between these two sites and Chimaera/Kidd Creek combined with the higher contribution of mantle helium reinforces the interpretation that methane from these two sites is abiotic in origin. The formation could have proceeded at temperatures slightly lower than those imposed by experimental constraints. Alternatively, post-formation resetting of abiotic methane isotopologues, dominated by changes in $\Delta^{12}\text{CH}_2\text{D}_2$ as described by Labidi et al. (2020b) might explain the shift from a purely abiotic isotopologue signature to one near equilibrium at lower temperatures, although the temperature disparity remains. The possibility that the abiogenic-like signatures are derived from AOM (Giunta et al., 2022; Warr et al., 2021, see Section 5.2 for more discussion), thermal maturation of organic matters circulated from surface waters (Fiebig et al., 2019) or biodegradation of organic matters with H_2 produced by serpentinization (Xia & Gao, 2021) is noted.

5.5. Water Isotopic Compositions

Isotopic compositions of water fell within the range reported previously (Chao et al., 2011; You et al., 2004). Among the data points, several sites LS and AT in the Coastal Range and site WF in the Chukou fault were distributed near or along the global and local meteoric water lines (Peng et al., 2010; Figure 4a). While data points for site GI clustered around a seawater composition (Table S5 in Supporting Information S1), all the other data points deviated from the meteoric water line and exhibited various degrees of ^{18}O enrichment (Figure 4a). By combining with previous results, two variation trends could be drawn. The first one is composed of data points for the Chishan fault, Gutingkeng anticline, and Coastal Plain, whereas the second one comprises data points solely from the Chukou fault. Both trends share a common end component enriched with ^{18}O ($\delta^{18}\text{O}_{\text{H}_2\text{O}}$ values were +7‰). The presence of such ^{18}O -enriched water was also observed in a previous study for the porewater retrieved from the TY mud volcano offshore southwestern Taiwan, and could best be accounted for by deep water derived from the smectite dehydration at 100°–150°C (N. C. Chen et al., 2020). Using the average geothermal gradient for the offshore region (25°C/km, Chi & Reed, 2008), the depth corresponding to the water formation has been estimated to range between 3.6 and 5.7 km below the seafloor (N. C. Chen et al., 2020). If this end component is prevalent in the accretionary wedge across the marine and terrestrial realms, the water mixture would be bracketed by three end components, including deep water (stated above), seawater-like water, and meteoric water.

For sites in the Chishan fault, Gutingkeng anticline, and Coastal Plain, the data distribution (Figure 4a) suggests a greater contribution of seawater-like water over meteoric water. Except for site TDS, most mud volcanoes in western Taiwan are located at least 10 km from the shoreline (Figure S1 in Supporting Information S1). Therefore, the scenario of the seawater intrusion is less likely. Instead, the seawater-like composition could have been derived from relic seawater trapped during sedimentation. In contrast, for sites in the Chukou fault, the data distribution is aligned clearly with an end component comparable with the compositions of meteoric water retrieved from the southern plain or mountains (Peng et al., 2010).

Finally, the involvement of an end component resembling meteoric water suggests a short residence time of water circulation. Constraining the exact age or residence time of water from mud volcanoes is challenging as the tracers available for such a geological context are limited, and no data have been published to date. Site LS was chosen as an example to constrain the potential limit for the circulation of meteoric water as its water isotopic compositions fell on the local meteoric water line. Based on the isotopologue abundances, the temperature and depth for methane formation for site LS were estimated to be up to 90°–100°C and 2–3 km below the land surface, respectively. If this depth limit to the circulation of meteoric water is also applied to all mud volcanoes in the Western Foothills, a fast-track path from the recharge of meteoric water to discharge along the fracture network at depths less than 3 km would be required. To accommodate this possibility, the fracture opening derived from the depressurization and thrust displacement related to the rapid uplift and erosion is speculated to enable bedrock to be more permeable for recharge and deep penetration of water. The inference might not be the unique cause for tectonically fragmented terrains with rapid uplift and erosion (Y. W. Chen et al., 2015; Dadson et al., 2003), as previous studies have demonstrated that isotopic compositions of cored calcite veins from a 2,000-m deep borehole (P. L. Wang et al., 2010) and hot springs sampled from northern Taiwan are indicative of meteoric in origin

(Chao et al., 2021; Lu et al., 2020). These results suggest that meteoric water could be recharged and circulated to deeper regions, heated up by the exhumed bedrocks that still preserve the relic heat associated with rapid uplift, and discharged along the fracture network to the surface outcrops.

The isotopic compositions of water suggest water circulation along different paths and the contribution of water compartmentalized in different source regions. For most samples from eastern Taiwan and few from western Taiwan, the meteoric nature further implied that water circulation is rapid with a short residence time in the subsurface. Therefore, the isotopic exchange between water and minerals is not substantially enough to alter the resultant water composition. In contrast, the majority of samples from western Taiwan bear the contribution of deep water that has experienced prolonged water-rock/mineral interactions. Water circulation along the divergent, and complex fracture network in the accretionary wedge enables the mixing process of deep water with either the formation water or meteoric water at shallow depths.

In addition to water origins, water isotopic compositions were used to constrain the source characteristics of both water and methane. Estimated temperatures based on deuterium exchange between water and methane were compared with those assessed by methane isotopologue abundances. The thermometer is adopted from Horibe and Craig (1995) using the following equation (for temperatures between 0° and 370°C):

$$\alpha(\text{H}_2\text{O}_{\text{Liq}}/\text{CH}_4) = 1.0997 + 8456/T^2 + 0.9611 \times 10^9/T^4 - 27.82 \times 10^{12}/T^6 \quad (8)$$

where α is the ratio of $^2\text{H}/^1\text{H}$ of water to methane, and T is in Kelvin.

For sites CLP, CLS, SYNH-02, and WD where isotopologue equilibrium is reached and deep water predominates over the other component, the temperatures estimated from the deuterium fractionations between methane and water ($\epsilon_{\text{CH}_4\text{-H}_2\text{O}}$) correspond closely to the temperatures predicted by $\Delta^{13}\text{CH}_3\text{D}$ and $\Delta^{12}\text{CH}_2\text{D}_2$ values (Figure 4, Table S5 in Supporting Information S1). Comparable temperature estimates could be obtained for two additional sites (sites SYNH-01, and LCW) if only $\Delta^{13}\text{CH}_3\text{D}$ values were considered. For the equilibrium fractionation associated with deuterium exchange, two phases (methane and water) were involved. Therefore, comparable temperature estimates deduced from isotopic substitution within a phase and between phases suggest that methane and water share a common source region, and the isotopic exchange between $^{13}\text{CH}_3\text{D}$ and water is more rapid than between $^{12}\text{CH}_2\text{D}_2$ and water. The $\Delta^{13}\text{CH}_3\text{D}/\Delta^{12}\text{CH}_2\text{D}_2$ values paired with $\epsilon_{\text{CH}_4\text{-H}_2\text{O}}$ values for all the other sites fell off the equilibrium line (Figure 4). Since methane and water from these sites represent a mixture of different sources, isotopic exchange within a phase or between phases after mixing does not reach equilibrium, possibly due to insufficient time or a kinetic barrier imposed by the relatively low temperature. Finally, temperature estimates based on paired isotopologue abundances were coherent for site LS in eastern Taiwan. However, the methane isotopologue abundances did not reach equilibrium with deuterium in the water. The data pattern contrasts with other studies (Giunta et al., 2019; D. T. Wang et al., 2015) and suggests that meteoric water percolating into the deep subsurface does not coexist with methane for a sufficiently long time or methane is not completely dissolved in water to achieve isotopic equilibrium between phases. Again, consistent with the interpretation based solely on water isotopic compositions, the water circulation is likely rapid, so the residence time is short.

5.6. Depth Constraints Using Isotopologue-Based Temperature Estimates

Our results indicated that the temperature estimates for sites CLP, CLS, KTL, SYNH-02, WD, and LS ranged from 99° to 260°C (Tables S2 and S6 in Supporting Information S1). Using measured local geothermal gradients (Chi & Reed, 2008) and assuming a surface temperature of 20°C, the methane generation depth was estimated to range from 2 to 9 km. The sites where methane reaches internal equilibrium are primarily distributed in three major structural features: sites CLP, CLS, and KTL in the Chukou fault, site SYNH-02 in the Chishan fault, and site LS in the Longitudinal Valley fault. The Chukou fault is an east dipping thrust oriented NE-SW (Yeh et al., 2016). Balanced cross sections suggest that the fault probably represents a complex fault system with subsurface branches forming an imbricate structure and an anticline underneath (Yeh et al., 2016). The fault and its branches are generally parallel to bedding within the Miocene formation and could be considered as part of the detachment fault extending to a depth of 7–8 km. The depth estimate ranged from 7 to 8 km for site CLP, to 4–5 km for site CLS, and to 6–8 km for site KTL (Figure 5a). As the formations are deformed and fragmented, water and gas transport could follow multiple routes interconnected each other. Therefore, the estimated depth

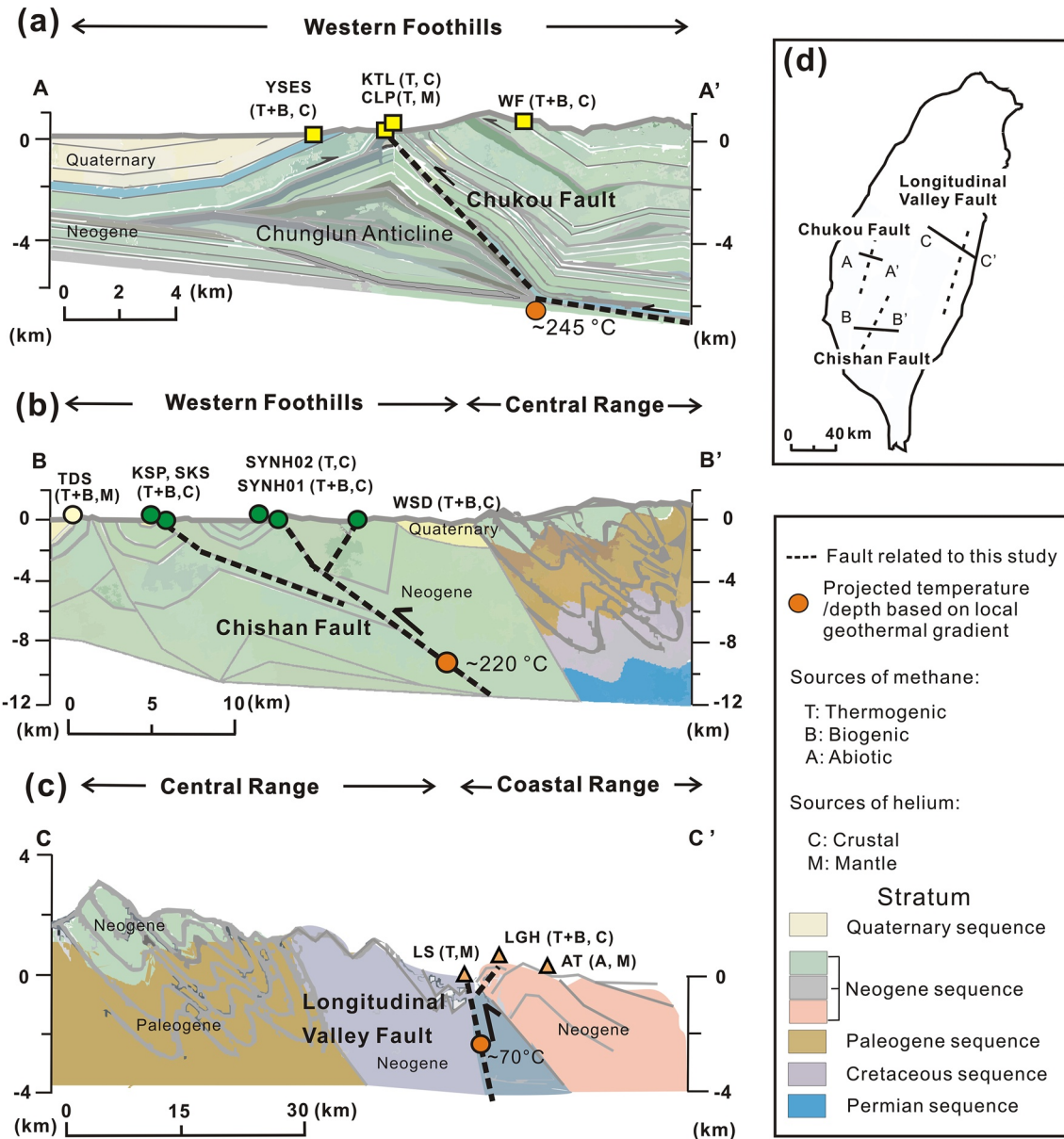


Figure 5. Schematic geological cross sections (modified from Chen (2016)) overlaid with the estimated depths of methane formation (solid orange circles) based on methane isotopologue abundances (this study) and local geothermal gradients (Chi & Reed, 2008) (Table S6 in Supporting Information S1). The geographic distribution of each cross section is excerpted from the solid lines in panel (d). Faults with the shearing sense related to individual structural domains are shown in black dashed lines with arrows. The estimated depths of methane formation are projected directly on the related faults to help visualize the possible two-dimensional range where methane is formed. Therefore, it is likely that the exact positions of methane formation deviate from the attributed fault systems (e.g., blind faults). Interpretations for the origins of methane and helium are also provided in parentheses next to site names with the first letter denoting for methane (T for thermogenic, B for biogenic, and A for abiotic) and the second letter for helium (C for crustal and M for mantle). Although the temperature (and depth) estimate (~190°C) based on two methane isotopologue abundances for site WD is available, no schematic cross section has been published due to the lack of subsurface geology data.

could be representative of the detachment fault and its related fracture system. For comparison, the Chishan fault is a high-angled, east dipping thrust with a left lateral component, and represents one of the branches of the detachment fault propagating westward (Rau et al., 2012). The depth estimates for site SYNH-02 were 8–9 km (Figure 5b), a range deeper than that reported for sampling in 2017 (Rumble et al., 2018; Supporting Information S1) and coinciding with the extension of the detachment fault (10–12 km) in the region (W. S. Chen, 2016). The occurrence is also consistent with the origin of ^{18}O -enriched water retrieved from sites SYNH-01 and -02. Site WD is located further west of site SYNH-02 in the Coastal Plain and is not associated with any apparent fault outcrop. Based on seismic reflection, mud diapirism oriented NE-SW offshore this region has

been identified (S. C. Chen et al., 2014). The site WD is aligned well with the onshore extension of one of the offshore mud diapirs. Whether the estimated formation depth of 7 km corresponds to the base of the mud diapir or the detachment fault remains uncertain. Regardless of the source characteristics, its water isotopic composition is comparable with that of site SYNH-02 and the designated deep water. Finally, the Longitudinal Valley fault is the plate boundary thrust with a high angle dipping east and a left lateral sense (C. P. Chang et al., 2000). The hanging wall formation (Lichi formation) hosts site LS, and is composed of unlithified clays with rock fragments of various lithologies (e.g., ultramafic, meta-sandstone) (W. S. Chen et al., 2007). This combined with intensive shearing suggests an intimate relationship with the subduction. The depth estimate of 2–3 km (Figure 5c) for this site probably corresponds to a source region at the base of the Lichi formation intersected by the Longitudinal Valley fault.

6. Conclusions

Our methane isotopologue results combined with helium, nitrogen, water, and CO₂ related isotopic compositions reveal a spectrum of geochemical characteristics that point to diverse formation mechanisms and conditions for gases and water emanating from mud volcanoes, seeps, and springs investigated. Thermogenic methane was formed at temperatures ranging between 99° and 260°C and appears to constitute a major component of hydrocarbons. The depths (2–9 km) corresponding to the estimated temperatures suggest a strong structural control that influences water and gas pathways. Thermogenic methane from a deep source is likely mixed to various degrees with abiogenic methane pertinent to igneous bodies emplaced during subduction/collision, or microbial methane at shallow depths prior to being discharged to the atmosphere or seawater. Our results also suggest the potential decoupling of methane from water or helium sources and an evolving depth range or mixing contribution for methane formation. Such patterns are consistent with active orogenesis, where gas and water channeling can undergo temporal and spatial variations associated with terrain fragmentation and dynamic structural control over the course of mountain building.

Data Availability Statement

All new data reported in the study are available on tables in the main manuscript and Supporting Information S1 and deposited in the Zenodo (<https://zenodo.org/record/8275042>).

References

- Ash, J. L., Egger, M., Treude, T., Kohl, I., Cragg, B., Parkes, R., et al. (2019). Exchange catalysis during anaerobic methanotrophy revealed by ¹²CH₂D₂ and ¹³CH₃D in methane. *Geochemical Perspectives Letters*, 26–30. <https://doi.org/10.7185/geochemlet.1910>
- Beaudry, P., Stefánsson, A., Fiebig, J., Rhim, J. H., & Ono, S. (2021). High temperature generation and equilibration of methane in terrestrial geothermal systems: Evidence from clumped isotopologues. *Geochimica et Cosmochimica Acta*, 309, 209–234. <https://doi.org/10.1016/j.gca.2021.06.034>
- Bernard, B. B., Brooks, J. M., & Sackett, W. M. (1977). A geochemical model for characterization of hydrocarbon gas sources in marine sediments. In *Paper presented at the offshore technology conference*. <https://doi.org/10.4043/2934-MS>
- Bohrmann, G., Berndt, C., Lin, S., Tu, T. H., Lin, A., Hsu, H. H., et al. (2023). Geological controls on the distribution of gas hydrates in the shallow parts of the gas hydrate stability zone—constraints from seafloor drilling off Taiwan. *Marine and Petroleum Geology*, 153, 106253. <https://doi.org/10.1016/j.marpetgeo.2023.106253>
- Busigny, V., Cartigny, P., & Philippot, P. (2011). Nitrogen isotopes in ophiolitic metagabbros: A re-evaluation of modern nitrogen fluxes in subduction zones and implication for the early Earth atmosphere. *Geochimica et Cosmochimica Acta*, 75(23), 7502–7521. <https://doi.org/10.1016/j.gca.2011.09.049>
- Campeau, A., Wallin, M. B., Giesler, R., Löfgren, S., Mörth, C. M., Schiff, S., et al. (2017). Multiple sources and sinks of dissolved inorganic carbon across Swedish streams, refocusing the lens of stable C isotopes. *Scientific Reports*, 7(1), 9158. <https://doi.org/10.1038/s41598-017-09049-9>
- Carson, B., & Sreaton, E. J. (1998). Fluid flow in accretionary prisms: Evidence for focused, time-variable discharge. *Reviews of Geophysics*, 36(3), 329–351. <https://doi.org/10.1029/97rg03633>
- Chang, C. P., Angelier, J., & Huang, C. Y. (2000). Origin and evolution of a mélange: The active plate boundary and suture zone of the Longitudinal Valley, Taiwan. *Tectonophysics*, 325(1–2), 43–62. [https://doi.org/10.1016/S0040-1951\(00\)00130-X](https://doi.org/10.1016/S0040-1951(00)00130-X)
- Chang, Y. H., Cheng, T. W., Lai, W. J., Tsai, W. Y., Sun, C. H., Lin, L. H., & Wang, P. L. (2012). Microbial methane cycling in a terrestrial mud volcano in eastern Taiwan. *Environmental Microbiology*, 14(4), 895–908. <https://doi.org/10.1111/j.1462-2920.2011.02658.x>
- Chao, H. C., Pi, J. L., You, C. F., Shieh, Y. T., Lu, H. Y., Huang, K. F., et al. (2021). Hydrogeology constrained by multi-isotopes and volatiles geochemistry of hot springs in Tatan Volcanic Group, Taiwan. *Journal of Hydrology*, 600, 126515. <https://doi.org/10.1016/j.jhydrol.2021.126515>
- Chao, H. C., You, C. F., Wang, B. S., Chung, C. H., & Huang, K. F. (2011). Boron isotopic composition of mud volcano fluids: Implications for fluid migration in shallow subduction zones. *Earth and Planetary Science Letters*, 305(1–2), 32–44. <https://doi.org/10.1016/j.epsl.2011.02.033>

Acknowledgments

We are grateful to the aid for sample and core retrievals by Nai-Chen Chen, Jui-Fen Tsai, Ling-Ho Chung, Tourism Bureau of Tainan City Government, Agriculture Bureau of Kaohsiung City Government, Zhaori Hot Spring of Taitung County Government, and the captain and crew members of R/V Sonne (cruise SO266/1). The MARUM-MeBo200 team and David Wunsch (CORSYDE International GmbH & Co. KG; Berlin) are sincerely thanked for the preparation and deployment of the MeBo pressure core samplers during cruise SO266/1. We extend our gratitude to Dr. George Burr at the National Taiwan University for English editing. Grant supports from Taiwanese Ministry of Education and Ministry of Science and Technology (MOST107-3113-M-002-004) are acknowledged. Cruise SO266/1 was funded by the German Ministry of Education and Science, project TaiDrill—SO266.

- Chasar, L., Chanton, J., Glaser, P. H., Siegel, D. I., & Rivers, J. S. (2000). Radiocarbon and stable carbon isotopic evidence for transport and transformation of dissolved organic carbon, dissolved inorganic carbon, and CH₄ in a northern Minnesota peatland. *Global Biogeochemical Cycles*, 14(4), 1095–1108. <https://doi.org/10.1029/1999GB001221>
- Chen, N. C., Yang, T. F., Hong, W. L., Chen, H., Chen, H., Hu, C., et al. (2017). Production, consumption, and migration of methane in accretionary prism of southwestern Taiwan. *Geochemistry, Geophysics, Geosystems*, 18(8), 2970–2989. <https://doi.org/10.1002/2017GC006798>
- Chen, N. C., Yang, T. F., Hong, W. L., Yu, T. L., Lin, I. T., Wang, P. L., et al. (2020). Discharge of deeply rooted fluids from submarine mud volcanism in the Taiwan accretionary prism. *Scientific Reports*, 10(1), 381. <https://doi.org/10.1038/s41598-019-57250-9>
- Chen, S. C., Hsu, S. K., Wang, Y., Chung, S. H., Chen, P. C., Tsai, C. H., et al. (2014). Distribution and characters of the mud diapirs and mud volcanoes off southwest Taiwan. *Journal of Asian Earth Sciences*, 92, 201–214. <https://doi.org/10.1016/j.jseas.2013.10.009>
- Chen, T. W., Chu, M. F., Chen, W. S., Chung, S., Lee, H., & Iizuka, Y. (2023). Retro-foredeep basin evolution in Taiwan: Zircon U-Pb and Hf isotope constraints from the coastal range. *Geochemistry, Geophysics, Geosystems*, 24(3), e2022GC010787. <https://doi.org/10.1029/2022GC010787>
- Chen, W. S. (2016). *An introduction to the geology of Taiwan*. Geological Society Located in Taipei.
- Chen, W. S., Yen, I. C., Fengler, K. P., Rubin, C., Yang, C., Yang, H., et al. (2007). Late Holocene paleoearthquake activity in the middle part of the Longitudinal Valley fault, eastern Taiwan. *Earth and Planetary Science Letters*, 264(3–4), 420–437. <https://doi.org/10.1016/j.epsl.2007.09.043>
- Chen, Y. W., Shyu, J. B. H., & Chang, C. P. (2015). Neotectonic characteristics along the eastern flank of the Central Range in the active Taiwan orogen inferred from fluvial channel morphology. *Tectonics*, 34(10), 2249–2270. <https://doi.org/10.1002/2014TC00379>
- Cheng, T. W., Chang, Y. H., Tang, S. L., Tseng, C. H., Chiang, P. W., Chang, K. T., et al. (2012). Metabolic stratification driven by surface and subsurface interactions in a terrestrial mud volcano. *The ISME Journal*, 6(12), 2280–2290. <https://doi.org/10.1038/ismej.2012.61>
- Chi, W. C., & Reed, D. L. (2008). Evolution of shallow, crustal thermal structure from subduction to collision: An example from Taiwan. *Geological Society of America Bulletin*, 120(5–6), 679–690. <https://doi.org/10.1130/b26210.1>
- Craig, H. (1961). Isotopic variations in meteoric waters. *Science*, 133(3465), 1702–1703. <https://doi.org/10.1126/science.133.3465.1702>
- Dadson, S. J., Hovius, N., Chen, H., Dade, W. B., Hsieh, M. L., Willett, S. D., et al. (2003). Links between erosion, runoff variability and seismicity in the Taiwan orogen. *Nature*, 426(6967), 648–651. <https://doi.org/10.1038/nature02150>
- Douglas, P. M., Stolper, D. A., Eiler, J. M., Sessions, A. L., Lawson, M., Shuai, Y., et al. (2017). Methane clumped isotopes: Progress and potential for a new isotopic tracer. *Organic Geochemistry*, 113, 262–282. <https://doi.org/10.1016/j.orggeochem.2017.07.016>
- Epstein, G. S., Bebout, G. E., Christenson, B. W., Sumino, H., Wada, I., Werner, C., & Hilton, D. R. (2021). Cycling of CO₂ and N₂ along the Hikurangi subduction margin, New Zealand: An integrated geological, theoretical, and isotopic approach. *Geochemistry, Geophysics, Geosystems*, 22(9), e2021GC009650. <https://doi.org/10.1029/2021GC009650>
- Etioppe, G. (2009). Natural emissions of methane from geological seepage in Europe. *Atmospheric Environment*, 43(7), 1430–1443. <https://doi.org/10.1016/j.atmosenv.2008.03.014>
- Etioppe, G., & Lollar, B. (2013). Abiotic methane on Earth. *Reviews of Geophysics*, 51(2), 276–299. <https://doi.org/10.1002/rog.20011>
- Fellin, M. G., Chen, C. Y., Willett, S. D., Christl, M., & Chen, Y. G. (2017). Erosion rates across space and timescales from a multi-proxy study of rivers of eastern Taiwan. *Global and Planetary Change*, 157, 174–193. <https://doi.org/10.1016/j.gloplacha.2017.07.012>
- Fiebig, J., Stefansson, A., Ricci, A., Tassi, F., Viveiros, F., Silva, S., et al. (2019). Abiogenesis not required to explain the origin of volcanic-hydrothermal hydrocarbons. *Geochimica et Cosmochimica Acta*, 233, 1–12. <https://doi.org/10.1016/j.gca.2019.07.012>
- Fu, C. C., Lai, C. W., Yang, T. F., Hilton, D. R., Chen, C. H., Wallia, V., et al. (2021). An automatic system for continuous monitoring and sampling of groundwater geochemistry in earthquake-prone regions of SW Taiwan. *Frontiers in Earth Science*, 9, 635913. <https://doi.org/10.3389/feart.2021.635913>
- Giunta, T., Labidi, J., Kohl, I. E., Ruffine, L., Donval, J., Géli, L., et al. (2021). Evidence for methane isotopic bond re-ordering in gas reservoirs sourcing cold seeps from the Sea of Marmara. *Earth and Planetary Science Letters*, 553, 116619. <https://doi.org/10.1016/j.epsl.2020.116619>
- Giunta, T., Young, E. D., Labidi, J., Sansjofre, P., Jézéquel, D., Donval, J. P., et al. (2022). Extreme methane clumped isotopologue bio-signatures of aerobic and anaerobic methanotrophy: Insights from the lake Pavin and the Black Sea sediments. *Geochimica et Cosmochimica Acta*, 338, 34–53. <https://doi.org/10.1016/j.gca.2022.09.034>
- Giunta, T., Young, E. D., Warr, O., Kohl, I., Ash, J. L., Martini, A., et al. (2019). Methane sources and sinks in continental sedimentary systems: New insights from paired clumped isotopologues ¹³CH₃D and ¹²CH₂D₂. *Geochimica et Cosmochimica Acta*, 245, 327–351. <https://doi.org/10.1016/j.gca.2018.10.030>
- Head, I. M., Jones, D. M., & Larter, S. R. (2003). Biological activity in the deep subsurface and the origin of heavy oil. *Nature*, 426(6964), 344–352. <https://doi.org/10.1038/nature02134>
- Horibe, Y., & Craig, H. (1995). DH fractionation in the system methane-hydrogen-water. *Geochimica et Cosmochimica Acta*, 59(24), 5209–5217. [https://doi.org/10.1016/0016-7037\(95\)00391-6](https://doi.org/10.1016/0016-7037(95)00391-6)
- Horita, J., & Wesolowski, D. J. (1994). Liquid-vapor fractionation of oxygen and hydrogen isotopes of water from the freezing to the critical temperature. *Geochimica et Cosmochimica Acta*, 58(16), 3425–3437. [https://doi.org/10.1016/0016-7037\(94\)90096-5](https://doi.org/10.1016/0016-7037(94)90096-5)
- Jautzy, J. J., Douglas, P. M., Xie, H., Eiler, J. M., & Clark, I. D. (2021). CH₄ isotopic ordering records ultra-slow hydrocarbon biodegradation in the deep subsurface. *Earth and Planetary Science Letters*, 562, 116841. <https://doi.org/10.1016/j.epsl.2021.116841>
- Karakashev, D., Batstone, D. J., Trably, E., & Angelidaki, I. (2006). Acetate oxidation is the dominant methanogenic pathway from acetate in the absence of Methanosetaeaceae. *Applied and Environmental Microbiology*, 72(7), 5138–5141. <https://doi.org/10.1128/AEM.00489-06>
- Kietäväinen, R., & Purkamo, L. (2015). The origin, source, and cycling of methane in deep crystalline rock biosphere. *Frontiers in Microbiology*, 6, 725. <https://doi.org/10.3389/fmicb.2015.00725>
- Kopf, A. J. (2003). Global methane emission through mud volcanoes and its past and present impact on the Earth's climate. *International Journal of Earth Sciences*, 92(5), 806–816. <https://doi.org/10.1007/s00531-003-0341-z>
- Krause, S. J., Liu, J., Young, E. D., & Treude, T. (2022). Δ¹³CH₃D and Δ¹²CH₂D₂ signatures of methane aerobically oxidized by *Methylosinus trichosporium* with implications for deciphering the provenance of methane gases. *Earth and Planetary Science Letters*, 593, 117681. <https://doi.org/10.1016/j.epsl.2022.117681>
- Labidi, J., Barry, P. H., Bekaert, D. V., Broadley, M. W., Marty, B., Giunta, T., et al. (2020a). Hydrothermal ¹⁵N/¹⁵N abundances constrain the origins of mantle nitrogen. *Nature*, 580(7803), 367–371. <https://doi.org/10.1038/s41586-020-2173-4>
- Labidi, J., & Young, E. (2022). The origin and dynamics of nitrogen in the Earth's mantle constrained by ¹⁵N/¹⁵N in hydrothermal gases. *Chemical Geology*, 591, 120709. <https://doi.org/10.1016/j.chemgeo.2022.120709>
- Labidi, J., Young, E. D., Fischer, T. P., Barry, P., Ballentine, C., & de Moor, J. (2021). Recycling of nitrogen and light noble gases in the Central American subduction zone: Constraints from ¹⁵N/¹⁵N. *Earth and Planetary Science Letters*, 571, 117112. <https://doi.org/10.1016/j.epsl.2021.117112>

- Labidi, J., Young, E. D., Giunta, T., Kohl, I., Seewald, J., Tang, H., et al. (2020b). Methane thermometry in deep-sea hydrothermal systems: Evidence for re-ordering of doubly-substituted isotopologues during fluid cooling. *Geochimica et Cosmochimica Acta*, 288, 248–261. <https://doi.org/10.1016/j.gca.2020.08.013>
- Lallemand, S. (2016). Philippine Sea Plate inception, evolution, and consumption with special emphasis on the early stages of Izu-Bonin-Mariana subduction. *Progress in Earth and Planetary Science*, 3(1), 15. <https://doi.org/10.1186/s40645-016-0085-6>
- Lee, Y. H., Byrne, T. B., Lo, W., Wang, S. J., Tsao, S. J., Chen, C. H., et al. (2022). Out of sequence faulting in the backbone range, Taiwan: Implications for thickening and exhumation processes. *Earth and Planetary Science Letters*, 594, 117711. <https://doi.org/10.1016/j.epsl.2022.117711>
- Lin, A. T., Liu, C. S., Lin, C. C., Schnurle, P., Chen, G. Y., Liao, W. Z., et al. (2008). Tectonic features associated with the overriding of an accretionary wedge on top of a rifted continental margin: An example from Taiwan. *Marine Geology*, 255(3–4), 186–203. <https://doi.org/10.1016/j.margeo.2008.10.002>
- Lin, Y. T., Tu, T. H., Wei, C. L., Rumble, D., Lin, L. H., & Wang, P. L. (2018). Steep redox gradient and biogeochemical cycling driven by deeply sourced fluids and gases in a terrestrial mud volcano. *FEMS Microbiology Ecology*, 94(11), 3796. <https://doi.org/10.1093/femsec/fiy171>
- Ling, Y. C., Chen, Y. J., Sun, C. H., Cheng, T. W., Wang, P. L., & Lin, L. H. (2012). Potential of microbial methane formation in a high-temperature hydrocarbon seep. *Applied Geochemistry*, 27(8), 1666–1678. <https://doi.org/10.1016/j.apgeochem.2012.04.002>
- Liu, C. S., Huang, I. L., & Teng, L. S. (1997). Structural features off southwestern Taiwan. *Marine Geology*, 137(3–4), 305–319. [https://doi.org/10.1016/S0025-3227\(96\)00093-X](https://doi.org/10.1016/S0025-3227(96)00093-X)
- Liu, J., Harris, R. L., Ash, J. L., Ferry, J. G., Krause, S. J., Labidi, J., et al. (2023). Reversibility controls on extreme methane clumped isotope signatures from anaerobic oxidation of methane. *Geochimica et Cosmochimica Acta*, 348, 165–186. <https://doi.org/10.1016/j.gca.2023.02.022>
- Lu, Y. C., Song, S. R., Lin, P. H., Taguchi, S., Wang, C., Lai, Y. M., et al. (2020). Thermal fluid changes after operating a geothermal system: A case study of the Chingshui geothermal field, Taiwan. *Geothermics*, 87, 101878. <https://doi.org/10.1016/j.geothermics.2020.101878>
- Lundegard, P. D., Sweeney, R. E., & Ririe, G. T. (2000). Soil gas methane at petroleum contaminated sites: Forensic determination of origin and source. *Environmental Forensics*, 1, 3–10. <https://doi.org/10.1006/enfo.1998.0002>
- Mazzini, A., & Etiope, G. (2017). Mud volcanism: An updated review. *Earth-Science Reviews*, 168, 81–112. <https://doi.org/10.1016/j.earscirev.2017.03.001>
- Milkov, A. V. (2011). Worldwide distribution and significance of secondary microbial methane formed during petroleum biodegradation in conventional reservoirs. *Organic Geochemistry*, 42(2), 184–207. <https://doi.org/10.1016/j.orggeochem.2010.12.003>
- Milkov, A. V., & Etiope, G. (2018). Revised genetic diagrams for natural gases based on a global dataset of >20,000 samples. *Organic Geochemistry*, 125, 109–120. <https://doi.org/10.1016/j.orggeochem.2018.09.002>
- Mishima, K., Sumino, H., Yamada, T., Ieki, S., Nagakura, N., Otono, H., & Oide, H. (2018). Accurate determination of the absolute $^3\text{He}/^4\text{He}$ ratio of a synthesized helium standard gas (helium standard of Japan, HESJ): Toward revision of the atmospheric $^3\text{He}/^4\text{He}$ ratio. *Geochimica et Cosmochimica Acta*, 19(10), 3995–4005. <https://doi.org/10.1029/2018GC007554>
- Ono, S., Rhim, J. H., Gruen, D. S., Taubner, H., Kölling, M., & Wegener, G. (2021). Clumped isotopologue fractionation by microbial cultures performing the anaerobic oxidation of methane. *Geochimica et Cosmochimica Acta*, 293, 70–85. <https://doi.org/10.1016/j.gca.2020.10.015>
- Ono, S., Rhim, J. H., & Ryberg, E. C. (2022). Rate limits and isotopologue fractionations for microbial methanogenesis examined with combined pathway protein cost and isotopologue flow network models. *Geochimica et Cosmochimica Acta*, 325, 296–315. <https://doi.org/10.1016/j.gca.2022.03.017>
- Ono, S., Wang, D. T., Gruen, D. S., Sherwood Lollar, B., Zahniser, M. S., McManus, B. J., & Nelson, D. D. (2014). Measurement of a doubly substituted methane isotopologue, $^{13}\text{CH}_3\text{D}$, by tunable infrared laser direct absorption spectroscopy. *Analytical Chemistry*, 86(13), 6487–6494. <https://doi.org/10.1021/ac5010579>
- Pape, T., Hohnberg, H. J., Wunsch, D., Anders, E., Freudenthal, T., Huhn, K., & Bohrmann, G. (2017). Design and deployment of autoclave pressure vessels for the portable deep-sea drill rig MeBo (Meeresboden-Bohrgerät). *Scientific Drilling*, 23, 29–37. <https://doi.org/10.5194/sd-23-29-2017>
- Peng, T. R., Wang, C. H., Huang, C. C., Fei, L. Y., Chen, C. T. A., & Hwong, J. L. (2010). Stable isotopic characteristic of Taiwan's precipitation: A case study of western Pacific monsoon region. *Earth and Planetary Science Letters*, 289(3–4), 357–366. <https://doi.org/10.1016/j.epsl.2009.11.024>
- Pepper, A. S., & Corvi, P. J. (1995). Simple kinetic models of petroleum formation. Part I: Oil and gas generation from kerogen. *Marine and Petroleum Geology*, 12(3), 291–319. [https://doi.org/10.1016/0264-8172\(95\)98381-E](https://doi.org/10.1016/0264-8172(95)98381-E)
- Poreda, R., & Craig, H. (1989). Helium isotope ratios in circum-Pacific volcanic arcs. *Nature*, 338(6215), 473–478. <https://doi.org/10.1038/338473a0>
- Rau, R. J., Lee, J. C., Ching, K. E., Lee, Y. H., Byrne, T. B., & Chen, R. Y. (2012). Subduction-continent collision in southwestern Taiwan and the 2010 Jishian earthquake sequence. *Tectonophysics*, 578, 107–116. <https://doi.org/10.1016/j.tecto.2011.09.013>
- Rouilleau, E., Sano, Y., Takahata, N., Yang, F. T., & Takahashi, H. A. (2015). He, Ar, N and C isotope compositions in Tatun Volcanic Group (TVG), Taiwan: Evidence for an important contribution of pelagic carbonates in the magmatic source. *Journal of Volcanology and Geothermal Research*, 303, 7–15. <https://doi.org/10.1016/j.jvolgeores.2015.07.017>
- Rumble, D., Ash, J. L., Wang, P. L., Lin, L. H., Lin, Y. T., & Tu, T. H. (2018). Resolved measurements of $^{13}\text{CDH}_3$ and $^{12}\text{CD}_2\text{H}_2$ from a mud volcano in Taiwan. *Journal of Asian Earth Sciences*, 167, 218–221. <https://doi.org/10.1016/j.jseaes.2018.03.007>
- Sano, Y., Tokutake, T., & Takahata, N. (2008). Accurate measurement of atmospheric helium isotopes. *Analytical Sciences: The international journal of the Japan Society for Analytical Chemistry*, 24(4), 521–525. <https://doi.org/10.2116/analsci.24.521>
- Schoell, M. (1988). Multiple origins of methane in the Earth. *Chemical Geology*, 71(1–3), 1–10. [https://doi.org/10.1016/0009-2541\(88\)90101-5](https://doi.org/10.1016/0009-2541(88)90101-5)
- Scholten, J. C., & Conrad, R. (2000). Energetics of syntrophic propionate oxidation in defined batch and chemostat cocultures. *Applied and Environmental Microbiology*, 66(7), 2934–2942. <https://doi.org/10.1128/AEM.66.7.2934-2942.2000>
- Shuai, Y., Douglas, P. M., Zhang, S., Stolper, D. A., Ellis, G. S., Lawson, M., et al. (2018). Equilibrium and non-equilibrium controls on the abundances of clumped isotopologues of methane during thermogenic formation in laboratory experiments: Implications for the chemistry of pyrolysis and the origins of natural gases. *Geochimica et Cosmochimica Acta*, 223, 159–174. <https://doi.org/10.1016/j.gca.2017.11.024>
- Stolper, D. A., Lawson, M., Davis, C. L., Ferreira, A. A., Neto, E. V. S., Ellis, G. S., et al. (2014). Formation temperatures of thermogenic and biogenic methane. *Science*, 344(6191), 1500–1503. <https://doi.org/10.1126/science.1254509>
- Stolper, D. A., Martini, A. M., Clog, M., Douglas, P., Shusta, S., Valentine, D., et al. (2015). Distinguishing and understanding thermogenic and biogenic sources of methane using multiply substituted isotopologues. *Geochimica et Cosmochimica Acta*, 161, 219–247. <https://doi.org/10.1016/j.gca.2015.04.015>
- Summons, R. E., Franzmann, P. D., & Nichols, P. D. (1998). Carbon isotopic fractionation associated with methylotrophic methanogenesis. *Organic Geochemistry*, 28(7–8), 465–475. [https://doi.org/10.1016/S0146-6380\(98\)00011-4](https://doi.org/10.1016/S0146-6380(98)00011-4)
- Sun, C. H., Chang, S. C., Kuo, C. L., Wu, J. C., Shao, P. H., & Oung, J. N. (2010). Origins of Taiwan's mud volcanoes: Evidence from geochemistry. *Journal of Asian Earth Sciences*, 37(2), 105–116. <https://doi.org/10.1016/j.jseaes.2009.02.007>

- Suppe, J. (1984). *Kinematics of arc-continent collision, flipping of subduction, and back-arc spreading near Taiwan* (Vol. 6, pp. 131–146). Geological Society of China Memoir.
- Takai, K., Nakamura, K., Toki, T., Tsunogai, U., Miyazaki, M., Miyazaki, J., et al. (2008). Cell proliferation at 122°C and isotopically heavy CH₄ production by a hyperthermophilic methanogen under high-pressure cultivation. *Proceedings of the National Academy of Sciences of the United States of America*, *105*(31), 10949–10954. <https://doi.org/10.1073/pnas.0712334105>
- Teng, L. S. (1987). Tectonostratigraphic facies and geo-logic evolution of the coastal range, eastern Tai-wan: Memoir of the geological society of China (Vol. 8, pp. 229–250).
- Teng, L. S., & Lin, A. T. (2004). Cenozoic tectonics of the China continental margin: Insights from Taiwan. *Geological Society, London, Special Publications*, *226*(1), 313–332. <https://doi.org/10.1144/gsl.Sp.2004.226.01.17>
- Wang, D. T., Gruen, D. S., Lollar, B. S., Hinrichs, K. U., Stewart, L. C., Holden, J. F., et al. (2015). Nonequilibrium clumped isotope signals in microbial methane. *Science*, *348*(6233), 428–431. <https://doi.org/10.1126/science.aaa4326>
- Wang, P. L., Chiu, Y. P., Cheng, T. W., Chang, Y. H., Tu, W. X., & Lin, L. H. (2014). Spatial variations of community structures and methane cycling across a transect of Lei-Gong-Hou mud volcanoes in eastern Taiwan. *Frontiers in Microbiology*, *5*, 121. <https://doi.org/10.3389/fmicb.2014.001>
- Wang, P. L., Wu, J. J., Yeh, E. C., Song, S. R., Chen, Y. G., & Lin, L. H. (2010). Isotopic constraints of vein carbonates on fluid sources and processes associated with the ongoing brittle deformation within the accretionary wedge of Taiwan. *Terra Nova*, *22*, 251–256. <https://doi.org/10.1111/j.1365-3121.2010.00940.x>
- Wang, Y., Lin, Y. N., Ota, Y., Chung, L., Shyu, J. B. H., Chiang, H., et al. (2022). Mud diapir or fault-related fold? On the development of an active mud-cored anticline offshore southwestern Taiwan. *Tectonics*, *41*(9), e2022TC007234. <https://doi.org/10.1029/2022TC007234>
- Warr, O., Young, E. D., Giunta, T., Kohl, I. E., Ash, J. L., & Sherwood Lollar, B. (2021). High-resolution, long-term isotopic and isotopologue variation identifies the sources and sinks of methane in a deep subsurface carbon cycle. *Geochimica et Cosmochimica Acta*, *294*, 315–334. <https://doi.org/10.1016/j.gca.2020.12.002>
- Whiticar, M. J. (1999). Carbon and hydrogen isotope systematics of bacterial formation and oxidation of methane. *Chemical Geology*, *161*(1–3), 291–314. [https://doi.org/10.1016/S0009-2541\(99\)00092-3](https://doi.org/10.1016/S0009-2541(99)00092-3)
- Xia, X., & Gao, Y. (2019). Kinetic clumped isotope fractionation during the thermal generation and hydrogen exchange of methane. *Geochimica et Cosmochimica Acta*, *248*, 252–273. <https://doi.org/10.1016/j.gca.2019.01.004>
- Xia, X., & Gao, Y. (2021). Methane from microbial hydrogenolysis of sediment organic matter before the great oxidation event. *Nature Communications*, *12*(1), 5032. <https://doi.org/10.1038/s41467-021-25336-6>
- Yang, T. F., Chen, C. H., Tien, R. L., Song, S., & Liu, T. (2003). Remnant magmatic activity in the coastal range of east Taiwan after arc-continent collision: Fission-track data and ³He/⁴He ratio evidence. *Radiation Measurements*, *36*(1–6), 343–349. [https://doi.org/10.1016/S1350-4487\(03\)00149-5](https://doi.org/10.1016/S1350-4487(03)00149-5)
- Yeh, Y. L., Strong, W., Chien, W. C., Chang, Y. Z., & Chen, C. H. (2016). Tomography of the Chukou Fault zone, southwest Taiwan: Insights from microearthquake data. *TAO: Terrestrial, Atmospheric and Oceanic Sciences*, *27*(3), 387. <https://doi.org/10.3319/TAO.2016.01.29.01>
- Yen, J. Y., Chen, K. S., Chang, C. P., & Boerner, W. M. (2008). Evaluation of earthquake potential and surface deformation by differential interferometry. *Remote Sensing of Environment*, *112*(3), 782–795. <https://doi.org/10.1016/j.rse.2007.06.012>
- Yeung, L. Y., Li, S., Kohl, I. E., Haslun, J. A., Ostrom, N. E., Hu, H., et al. (2017). Extreme enrichment in atmospheric ¹⁵N/¹⁵N. *Science Advances*, *3*(11), 6741. <https://doi.org/10.1126/sciadv.aao6741>
- You, C. F., Gieskes, J. M., Lee, T., Yui, T. F., & Chen, H. W. (2004). Geochemistry of mud volcano fluids in the Taiwan accretionary prism. *Applied Geochemistry*, *19*(5), 695–707. <https://doi.org/10.1016/j.apgeochem.2003.10.004>
- Young, E. D., Kohl, I. E., Lollar, B. S., Etiope, G., Rumble, D., Li 李妹宁, S., et al. (2017). The relative abundances of resolved ¹²CH₂D₂ and ¹³CH₃D and mechanisms controlling isotopic bond ordering in abiotic and biotic methane gases. *Geochimica et Cosmochimica Acta*, *203*, 235–264. <https://doi.org/10.1016/j.gca.2016.12.041>
- Young, E. D., Rumble, D., Freedman, P., & Mills, M. (2016). A large-radius high-mass-resolution multiple-collector isotope ratio mass spectrometer for analysis of rare isotopologues of O₂, N₂, CH₄ and other gases. *International Journal of Mass Spectrometry*, *401*, 1–10. <https://doi.org/10.1016/j.ijms.2016.01.006>

References From the Supporting Information

- Bonilla, M. G. (1975). A review of recently active faults in Taiwan: U.S. Geological survey open-file report 75-41 version 1.1. Central Geological Survey. (2023). Retrieved from <https://twgeoref.moeacgs.gov.tw>
- Central Weather Bureau. (2023). Retrieved from <https://scweb.cwb.gov.tw/en-US/earthquake/details/2017021101125257008>
- Chao, H. C., You, C. F., & Sun, C. H. (2010). Gases in Taiwan mud volcanoes: Chemical composition, methane carbon isotopes, and gas fluxes. *Applied Geochemistry*, *25*(3), 428–436. <https://doi.org/10.1016/j.apgeochem.2009.12.009>
- Chen, A. T., Sano, Y., Byrne, T. B., Takahata, N., Yang, T. F., Wang, Y., & Shen, C. C. (2020). Helium isotopic signature of a plate boundary suture in an active arc-continent collision. *Earth and Space Chemistry*, *4*(8), 1237–1246. <https://doi.org/10.1021/acsearthspacechem.0c00038>
- Chen, S. C., Hsu, S. K., Tsai, C. H., Ku, C. Y., Yeh, Y. C., & Wang, Y. (2010). Gas seepage, pockmarks and mud volcanoes in the near shore of SW Taiwan. *Marine Geophysical Researches*, *31*(1–2), 133–147. <https://doi.org/10.1007/s11001-010-9097-6>
- Chung, S. L., Yang, T. F., Lee, C. Y., & Chen, C. H. (1995). The igneous provinciality in Taiwan: Consequence of continental rifting superimposed by Luzon and Ryukyu subduction systems. *Journal of Southeast Asian Earth Sciences*, *11*(2), 73–80. [https://doi.org/10.1016/0743-9547\(94\)00040-L](https://doi.org/10.1016/0743-9547(94)00040-L)
- Chyi, L. L., Chou, C. Y., Yang, F. T., & Chen, C.-H. (2001). Continuous radon measurements in faults and earthquake precursor pattern recognition. *Western Pacific Earth Sciences*, *1*, 227–246.
- Huang, S. T., Yang, K. M., Hung, J. H., Wu, J. C., Ting, H. H., Mei, W. W., et al. (2004). Deformation front development at the northeast margin of the Tainan basin, Tainan–Kaohsiung area, Taiwan. *Marine Geophysical Researches*, *25*(1–2), 139–156. <https://doi.org/10.1007/s11001-005-0739-z>
- Klaucke, I., Berndt, C., Crutchley, G., Chi, W. C., Lin, S., & Muff, S. (2016). Fluid venting and seepage at accretionary ridges: The Four Way Closure Ridge offshore SW Taiwan. *Geo-Marine Letters*, *36*(3), 165–174. <https://doi.org/10.1007/s00367-015-0431-5>
- Kunath, P., Chi, W. C., Berndt, C., Chen, L., Liu, C., Kläschen, D., & Muff, S. (2020). A shallow seabed dynamic gas hydrate system off SW Taiwan: Results from 3-D seismic, thermal, and fluid migration analyses. *Journal of Geophysical Research: Solid Earth*, *125*(11), e2019JB019245. <https://doi.org/10.1029/2019JB019245>

- Kunath, P., Crutchley, G., Chi, W. C., Berndt, C., Liu, C., Elger, J., et al. (2022). Episodic venting of a submarine gas seep on geological time scales: Formosa Ridge, northern South China Sea. *Journal of Geophysical Research: Solid Earth*, *127*(9), e2022JB024668. <https://doi.org/10.1029/2022JB024668>
- Lacombe, O., Mouthereau, F., Deffontaines, B., Angelier, J., Chu, H. T., & Lee, C. T. (1999). Geometry and Quaternary kinematics of fold-and-thrust units of southwestern Taiwan. *Tectonics*, *18*(6), 1198–1223. <https://doi.org/10.1029/1999TC900036>
- Lai, L. S. H., Roering, J. J., Finnegan, N. J., Dorsey, R. J., & Yen, J. (2021). Coarse sediment supply sets the slope of bedrock channels in rapidly uplifting terrain: Field and topographic evidence from eastern Taiwan. *Earth Surface Processes and Landforms*, *46*(13), 2671–2689. <https://doi.org/10.1002/esp.5200>
- Sano, Y., Kinoshita, N., Kagoshima, T., Takahata, N., Sakata, S., Toki, T., et al. (2017). Origin of methane-rich natural gas at the West Pacific convergent plate boundary. *Scientific Reports*, *7*, 1–10. <https://doi.org/10.1038/s41598-017-15959-5>
- Shao, W. Y., Chung, S. L., & Chen, W. S. (2014). Zircon U-Pb age determination of volcanic eruptions in Lutaio and Lanyu in the northern Luzon magmatic arc. *Terrestrial Atmospheric and Oceanic Sciences*, *25*(2), 149. [https://doi.org/10.3319/TAO.2013.11.06.01\(TT\)](https://doi.org/10.3319/TAO.2013.11.06.01(TT))
- Tseng, Y., Römer, M., Lin, S., Pape, T., Berndt, C., Chen, T. T., et al. (2023). Yam seep at four-way Closure Ridge: A prominent active gas seep system at the accretionary wedge SW offshore Taiwan. *International Journal of Earth Sciences*, *112*(3), 1043–1061. <https://doi.org/10.1007/s00531-022-02280-4>
- Yang, T. F., Yeh, G. H., Fu, C. C., Wang, C. C., Lan, T. F., Lee, H. F., et al. (2004). Composition and exhalation flux of gases from mud volcanoes in Taiwan. *Environmental Geology*, *46*(8), 1003–1011. <https://doi.org/10.1007/s00254-004-1086-0>
- Yu, H. S., & Chang, E. T. Y. (2009). Links among slope morphology, canyon types and tectonics on passive and active margins in the northernmost South China Sea. *Journal of Earth Sciences*, *20*(1), 77–84. <https://doi.org/10.1007/s12583-009-0008>